View Article Online
View Journal

Green Chemistry

Cutting-edge research for a greener sustainable future

Accepted Manuscript

This article can be cited before page numbers have been issued, to do this please use: Y. Song, J. Wang, J. Zhou, X. Wang, C. Unluer, T. Shi, A. Zhang, C. Chang and S. Ruan, *Green Chem.*, 2025, DOI: 10.1039/D5GC03502C.

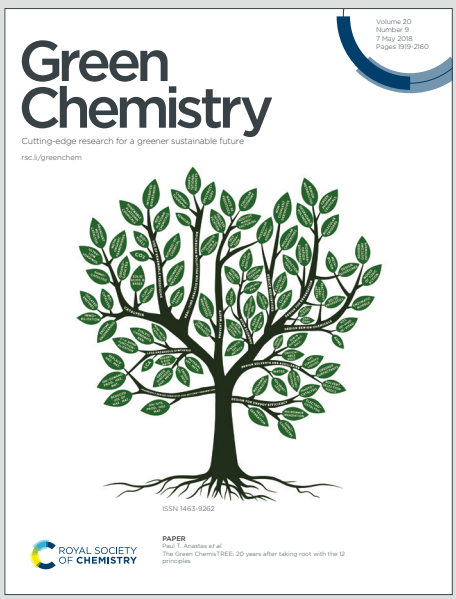

View Article Online
DOI: 10.1039/D5GC03502C

1. How does your work advance the field of green chemistry?

Transforming waste bischofite brine into reactive magnesia cement (RMC), reducing reliance on virgin magnesite and mitigating environmental impact from brine disposal. The resulting CO_2-cured mortar actively sequesters carbon, offering a carbon-storing alternative to Portland cement.

2. Please can you describe your specific green chemistry achievement, either quantitatively or qualitatively?

Synthetic RMC-based mortar exhibits 19.7% lower CO_2 emissions per MPa than commercial RMC mortar. This combines waste utilization (bischofite), reduced process emissions compared to literature wet synthesis (-18.9%), and significant CO_2 uptake during curing.

3. How could your work be made greener and be elevated by further research?

Replace the carbon-intensive CaO alkaline source with lower-impact alternatives (e.g., alkaline wastewater from concrete mixing plant). Optimize carbonation curing conditions to maximize CO_2 uptake.

Technical and carbon footprint assessment of mortars derived from CO_2 and magnesia recovered from bischofite

View Article Online
DOI: 10.1039/D5GC03502C

Yufeng Song[a,b], Jiaze Wang[b], Xinpeng Wang[a], Jiahao Zhou[b], Cise Unluer[c], Tao Shi[a], Aoyun Zhang[b], Chenggong Chang[d,e], Shaoqin Ruan[b,*]

[a] College of Civil Engineering, Zhejiang University of Technology, Hangzhou 310023, China

[b] College of Civil Engineering and Architecture, Zhejiang University, Hangzhou 310058, China

[c] Department of Civil Engineering and Management, University of Manchester, Manchester M13 9PL, United Kingdom

[d] Key Laboratory of Comprehensive and Highly Efficient Utilization of Salt Lake Resources, Qinghai Institute of Salt Lake, Chinese Academy of Sciences, Xining 810008, China

[e] Key Laboratory of Salt Lake Resources Chemistry of Qinghai Province, Xining 810008, China

***Corresponding author:** sruan001@zju.edu.cn

Abstract

Bischofite ($MgCl_2 \cdot 6H_2O$), the byproduct of salt lake resource extraction, is a useful source for valuable resources. This study investigated the production and utilization of reactive magnesia (MgO) cement (RMC) from bischofite. Synthetic RMC recovered through timed calcination was used in preparing CO_2-cured mortar and compared to samples produced from commercial RMC. The acid neutralization time, an indication of reactivity, of the

synthetic RMC from complete calcination indicated a good correlation with specific surface area. Synthetic RMC-based mortars exhibited higher reaction rates of hydration and carbonation than mortars involving commercial RMC. Furthermore, mortars prepared with synthetic RMC demonstrated higher compressive strengths, attributed to a denser pore structure and enhanced moduli/hardness in interfacial transition zone. The indentification of the key factors governing mechanical performance facilitated the regulation of the strength of high-activity RMC-based mortars. The overall CO_2 per MPa of the synthetic MgO-based mortar was 19.7% lower than that for the commercial RMC-based mortar.

Keywords: waste brine; synthetic magnesia; calcination; pore structures; nanoindentation; life cycle assessment (LCA)

1 Introduction

Ordinary Portland cement (OPC), a primary component of concrete, poses significant environmental challenges due to the high CO_2 emissions associated with its production [1-4]. Much research has focused on low-carbon alternatives to achieve carbon neutrality, with reactive magnesia cement (RMC) emerging as a promising substitute for OPC [5-7]. RMC is produced by decomposing magnesite (~700-900 °C, dry route) or brucite (~500−700 °C, wet route) [8]. However, the limited availability of magnesite restricts global access and increases costs. In contrast, abundant magnesium resources in Qinghai Lake, China, offer a more accessible and cost-effective alternative. Unfortunately, the extraction of potassium salts generates a large amount of magnesium-rich byproduct, bischofite ($MgCl_2 \cdot 6H_2O$), which remains underutilized and contributes to environmental degradation [9]. Consequently, recovering RMC from bischofite presents an attractive option for producing RMC with reduced environmental impacts [1], and recent studies have demonstrated the feasibility of using bischofite for RMC production [10, 11].

View Article Online
DOI: 10.1039/D5GC03502C

Researchers have precipitated $Mg(OH)_2$ by adding alkali to seawater or brine, primarily focusing on the effects of different alkali sources, calcination temperatures, and times on RMC characteristics, such as reactivity [12-14]. Among various alkali sources used for precipitating $Mg(OH)_2$ from desalination brine, CaO is noted for its lowest environmental impact [15]. Studies also show that $Mg(OH)_2$ precursors can be calcined at 500 °C for 2 h to obtain highly reactive magnesia. However, a significant decrease in RMC reactivity is observed with increasing calcination temperatures within the 400-550 °C range, particularly above 500 °C [14]. In investigations of calcination temperature and time effects on magnesia properties, the predominant method used is timed calcination, which involves controlled heating for a specified duration without an intervening cooling phase [12, 13]. This method is less effective for energy conservation and emission reduction.

In addition to rejecting brine, other magnesium-rich sources can also be used to produce magnesia. For instance, Badjatya [1] utilized membrane-free electrolyzers to convert Mg^{2+} in seawater into $Mg(OH)_2$, which was then calcined to obtain MgO. Zheng [16] produced MgO by sintering bischofite at 1000, 1050, 1100, and 1150 °C for 1, 2, and 3 hours. Most research has focused on RMC-based concrete [2, 17, 18], while studies on RMC-based mortar are less common [7], especially those exploring the use of precipitated $Mg(OH)_2$ or synthetic RMC for mortar preparation [19, 20]. Despite the improved strength observed in concrete with a lower w/b ratio within the 0.55-0.65 range [18], differences in mix proportions and pore structure between RMC-based mortar and concrete complicate the understanding of how w/b ratio influences the carbonation degree and strength of RMC-based mortar.

Compared to concrete, mortar mixes typically have a higher water-to-binder (w/b) ratio [21], which increases their porosity and makes them more susceptible to CO_2 penetration. Conversely, coarse aggregates in concrete can slow CO_2 penetration [22]. Therefore, the

CO_2 diffusion patterns differ between RMC-based mortar and concrete. Additionally, our previous work [20] showed that the interfacial transition zone (ITZ) in synthetic RMC-based mortar is denser than in commercial RMC-based mortar, leading to superior mechanical properties. In OPC-based mortar mix design, the mortar strength primarily depends on the cement strength and w/c ratio for non-absorbent substrates. Conversely, for absorbent substrates, the strength depends mainly on the cement strength and content, with less influence from the w/c ratio. However, the lack of a clear quantitative relationship between pore structure, ITZ characteristics, and RMC-based mortar strength at the microscale hinders the optimization of mortar formulations and CO_2-curing regimes.

Based on these considerations, the brine from potassium extraction at Caerhan Salt Lake, which primarily contains bischofite, was effectively used to produce highly reactive synthetic RMC. Two calcination regimes, timed calcination and complete calcination, were innovatively employed to calcinate $Mg(OH)_2$ extracted from the brine. This study is the first to elucidate the relation between lattice transformation of $Mg(OH)_2$ calcined at 400, 500 and 600 °C and reactivity of RMC. Both synthetic and commercially available RMC were then used to prepare mortar samples with varying w/c ratios, which were then subjected to a 28-day CO_2 curing period. The underlying mechanisms of strength development and key controlling factors were revealed to explain the differences between synthetic and commercial RMC-based mortars by using microscopic characterization techniques, including X-ray diffraction (XRD), thermogravimetric and differential thermogravimetric Analysis (TG-DTG), X-ray computed tomography (X-CT), and nanoindentation. Finally, the carbon footprint of commercial and synthetic RMC was analyzed using the single indicator IPCC 2013 GWP 100a, yielding the global warming potential of each product, as well as incorporating the CO_2 sequestration level and mechanical performance of mortars prepared with each binder.

2 Materials, sample preparation and methodology

2.1 RMC synthesis

View Article Online
DOI: 10.1039/D5GC03502C

Fig. 1 (a) illustrates the process for preparing synthetic RMC and mortars. The brine, mainly composed of bischofite, is a byproduct of potassium extraction from Caerhan Salt Lake. The specific composition of the brine is detailed in **Table S1** of supplement document. To achieve a 0.15 mol/L Mg^{2+} concentration, bischofite was dissolved in water. CaO, a cost-effective alkali source, was used to extract $Mg(OH)_2$, maintaining a Ca^{2+}/Mg^{2+} molar ratio of 1. Initially, CaO was added to 200 mL of brine, ultrasonically dispersed for 3 minutes, and stirred to ensure complete dissolution [1]. The resulting solution was transferred to a 25 L reaction tank containing brine, and manually shaken every hour for 5 mins, with the pH monitored until stabilization, indicating reaction completion. After 24 h of natural separation, the solid accumulated at the tank bottom was separated from the solution.

The newly formed precipitates and liquid were separated using a centrifuge. The solid phases were washed three times with deionized water, repeating the solid-liquid separation step after each wash. The washed $Mg(OH)_2$ solids were placed in an oven at 105 °C for one day. After drying, the solids were ground into powder under consistent grinding conditions to ensure uniform grain size distribution across different batches [1].

The microscopic morphology, XRD pattern, and particle size distribution of brucite are shown in **Fig. S1 (a)-(c)** in the Supplementary documents. Brucite appeared as nanoflake particles with rounded and cornered edges, with most particle sizes ranging between 50 and 200 nm (**Fig. S1 (a)**). A faint impurity peak, likely calcite, was also observed in (**Fig. S1 (b)**). Rietveld refinement results indicated that the $Mg(OH)_2$ (brucite) content exceeded 94%, confirming the effectiveness of the preparation process. Two calcination schemes were employed to produce RMC from $Mg(OH)_2$ (see **Table 1**), with details outlined below:

(1) RMC-TC via timed calcination: Calcination was maintained for 1 or 2 h after reaching the maximum temperature, following the method described in reference [14]. The groups were labeled as Sx-1 or Sx-2. For example, S4-1 represents the RMC obtained after calcination at 400 °C for 1 h.

(2) RMC-CC via complete calcination: Calcination continued for 0, 0.5, or 6 h after reaching the maximum temperature. The heat source was then turned off, allowing the furnace to cool naturally for 24 h. The parameters (calcination temperature and holding time) were based on relevant literature [12, 14]. Additionally, SS7-6 was designated as the over-calcined group due to its maximum temperature (700 °C) and prolonged holding time (6 hours), which significantly exceeded those of other groups.

Brucite was heated in a 100 mm × 100 mm × 25 mm alumina crucible with a 4 mm thickness, using a heating rate of 20 °C/min. **Fig. 1 (b)** demonstrates the calcination temperature curves for the S4-1 and SS5-0.5 groups over time.

2.2 Sample preparation

In addition to using synthetic RMC as the binder for mortar, the study included another binder, commercial RMC derived from calcined magnesite, serving as the control group. The specific surface area (SSA) of the commercial RMC, determined through Brunauer Emmett Teller (BET) testing, was 12.4 m²/g. The acid neutralization time, assessed in accordance with YB/T 4019—2020 [23], was 1033 s. The chemical composition of the commercial RMC was: MgO: 93.66%, SiO_2: 3.28%, CaO: 1.62%, Fe_2O_3: 0.59%, Al_2O_3: 0.30%, and SO_3: 0.14%. For mortar formulation, river sand (~diameter: 1.30-2.36 mm) was used as fine aggregate, with its grading curve shown in **Fig. S1 (d)** of supplement document.

Table 2 presents the mixture details of RMC-based mortar, with RMC-TC and commercial

View Article Online
DOI: 10.1039/D5GC03502C

RMC used in the preparation. Initially, RMC and sand were combined, followed by gradual water addition during mixing until a homogeneous mixture was achieved. The mortar fluidity was tested using the jumping table method as per standard [24]. The fresh slurry was cast into cubic molds measuring 13 mm × 13 mm × 13 mm (within the 10-20 mm size range in the literatures [1, 19, 20]), compacted with a vibrating table, and leveled. The mold diameter (~13 mm) was 5.5 times the maximum sand diameter (~2.36 mm), ensuring optimal performance and strength of the mortars. Subsequently, all specimens underwent CO_2 curing (CO_2 concentration: 20±2%; Relative humidity: 60±5%; Temperature: 20±2 °C) [18, 25] in an HTX-12X chamber (Donghua Examination Apparatus, China). After 1 d, specimens were demolded and continued curing under carbonation conditions for up to 28 d.

2.3 Methodology

After completing the calcination process illustrated in section 2.1, the RMC powder was stored in a sealed bag for subsequent physicochemical properties tests. Besides, microstructural analysis of specimens was conducted on samples obtained at 3 days and 14 days, following established references [17, 18]. Paste segments extracted from the interior region of the specimens after compression testing were utilized for the microstructural analysis. These paste segments were immersed in ethanol for 3 days to arrest hydration [26], followed by vacuum drying (~40 °C) for an additional 3 days. Post-drying, the specimens were used for the nanoindentation test, and other specimens were ground to pass through a 75 μm sieve for tests of XRD and TG.

2.3.1 Physical properties of commercial and synthetic RMC

The crystallite size, particle size, specific surface area, reactivity, and morphologies of RMC were measured as follows:

(a) Crystallite size: X-ray diffraction (XRD) analysis was conducted using a Bruker D8

View Article Online
DOI: 10.1039/D5GC03302C

Advance diffractometer, operating at 40 kV and 40 mA with Cu-Kα radiation. The scanning range was from 5° to 90° 2θ, with a step size of 0.02°. The crystallite size of synthetic RMC was calculated using the Scherrer formula [27-29], as shown in Eq. (1):

$$G_{xrd} = \frac{K\lambda}{\beta \times \mathrm{Cos}\theta} \quad (1)$$

where G_{xrd} is the crystallite size (nm); K is the Scherrer constant (0.89); λ Is the X-ray wavelength (0.1541 nm for Cu-Kα); β is the full width at half maxima (rad); and θ is the diffraction angle.

(b) Particle size: 50 mg RMC powder was sonicated in 20 mL anhydrous ethanol for 3 minutes, and then the particle size of RMC was investigated by laser diffraction method using Beckman–Coulter LS 13320 laser particle analyzer.

(c) SSA: The SSA of RMC was obtained by Brunauer-Emmett-Teller (BET) method by using Micromeritics ASAP 2020 HD88. Before the test, the powder was degassed at 150 °C for 10 hours. RMC reactivity was tested in line with YB/T 4019-2020 [30].

(d) Reactivity: At a 40 °C temperature and a 700 rpm magnetic stirring rate, 1.70 g RMC was used to neutralize 200 mL citric acid solution (0.07 mol/L, containing 4 drops of phenolphthalein indicator). The time (s) required for neutralization were measured. The two parallel samples were tested for each group and the average value was recorded.

(e) Morphologies: Scanning electron microscopy (SEM) was used to observe the morphologies of RMC. Before analysis, RMC samples were mounted on conductive adhesives for observation using an SU 8010 SEM (Hitachi, Japan) at 15 kV and a working distance of 9.5 mm.

2.3.2 Mechanical properties of RMC-based mortar

View Article Online
DOI: 10.1039/D5GC03302C

The compressive strength of RMC-based mortar is a crucial indicator for evaluating material performance, ensuring the safety of building structures, maintaining quality control, and optimizing economic efficiency. Additionally, nanoindentation testing allows for analyzing RMC-based mortar's performance variations at the microscale, providing insights into the relationship between its internal microstructure and mechanical properties. This technique can precisely target different areas within RMC-based mortar, especially the interfacial transition zone (ITZ), thereby revealing the performance characteristics of the interface region.

(a) Compressive strength: The compressive strength of the mortar was assessed using an AI-7000M servo-controlled tensile testing machine at a loading rate of 0.5 mm/min [1]. Each group was tested in triplicate, and the results were reported as the average and standard deviation.

(b) Elastic modulus and hardness: To determine the elastic modulus and hardness of the mortar, nanoindentation was employed. Specimens were impregnated with a fast-hardening epoxy solution in cylindrical molds (Diameter: 25 mm; Height: 50 mm). The demolded specimens were then ground and polished using an Ecomet 250 grinder/polisher, following the procedures outlined in the reference [18]. Silicon carbide sandpaper with particle sizes of 180, 600, 1200, and 2000 was used for rough grinding, processing each group for 5 minutes. Subsequently, the specimens were polished sequentially with 3, 1, and 0.25 μm diamond spray polishing agents for 15 minutes each. The turntable and base rotational speeds were maintained at 30 r/min, and a loading force of 5 N was applied.

The specimen's root mean square (RMS) roughness was measured using the NT9100 profiler, with the selected area size set at 63×47 μm. Additionally, five positions near the interfacial transition zone (ITZ) were assessed in each group to calculate the average value.

View Article Online
DOI: 10.1039/D5GC03502C

The average indentation depth (436 nm) was approximately four times the average RMS roughness (104 nm), indicating that roughness effects on the measured properties were mitigated.

In the ITZ grid nanoindentation tests, an Agilent G200 nanoindentation tester was used with a maximum load of 2 mN. The loading (t_L), unloading (t_U), and maximum load holding durations (t_H) were set at 10 s, 10 s, and 5 s, respectively. The horizontal and vertical spacing between adjacent indentation points was 20 μm, covering a grid range of 100×180 μm. Further details of the test procedure are outlined in our previous research [18].

2.3.3 Hydration/carbonation degrees of RMC-based mortar

X-ray diffraction (XRD) and thermogravimetric-differential thermogravimetric analysis (TG-DTG) were employed to measure the hydration and carbonation degrees of RMC-based mortar.

For RMC-based mortar, the RIR method [31] was employed for quantitative phase analysis using a fluorite internal standard material of 20 wt% CaF_2. The weight fractions of MgO and Mg(OH) were calculated using the equation y = kx, where x represents the RIR of the phase being analyzed (determined by dividing the integrated intensity of the phase's strongest line by that of fluorite) [31], and y is the weight fraction of MgO or $Mg(OH)_2$. The k values are 0.2886 for MgO and 0.3651 for $Mg(OH)_2$ [32]. Each test was conducted twice, and the average value was recorded.

The TG-DTG test was used to investigate the hydration and carbonation degree of RMC-based mortar, using a TGA2 (Mettler Toledo Crop., Switzerland). The test involved heating from 30 to 1000 °C at a 10 °C/min rate [33] with a nitrogen flow of 50 mL/min.

2.3.4 Pore structure of RMC-based mortar

X-ray Computed Tomography (X-CT) analyses were performed using the Nikon XTH320 at 180 kV and 220 μA. Two thousand projections were collected from various angles as the specimen rotated uniformly by 360°, with an exposure time of 0.5 seconds per projection. CTPro and VGStudio software were then used to generate gray images and conduct pore analysis, respectively, as described in reference [2]. The grey value range method was employed to distinguish the pore phase by identifying the lower grey values of the low-density phase from the higher ones of the high-density phase. The resulting X-CT images had a pixel resolution of 3.3 μm/pixel.

View Article Online
DOI: 10.1039/D5GC03502C

2.3.5 Correlation analysis

Correlation analysis is a statistical method employed to elucidate the relationships between different parameters and quantify their degree of association. In this study, the Pearson correlation coefficient was employed as the metric to evaluate these relationships. A greater absolute value of the Pearson correlation coefficient indicates a stronger association between the variables. The Pearson correlation coefficients in this research were calculated using the statistical software packages Origin and SPSS.

2.3.6 Carbon footprint assessment

This section analyzes the carbon emissions of the wet synthesis route for RMC compared to the conventional production process of commercial RMC, and extends the analysis to the mortar level. The specific analytical methods are based on the ISO 14040 and 14044 standards, corresponding to the GB/T 24040 and 24044. The assessment was conducted using the LCA software SimaPro 9.0, with details of system boundary, functional unit and life cycle inventories of RMC through dry and wet routes were illustrated in **Text S1** in Supplementary documents.

3 Results and discussion

3.1 Physical properties of synthetic RMC

XRD, SEM, laser diffraction method, BET and citric acid neutralization method [30] were used to investigate the crystallite size, morphologies, SSA, particle size and reactivity, respectively.

3.1.1 Crystallite size

The hexagonal structure of $Mg(OH)_2$ transforms into the regular structure of MgO while preserving the anionic planes of the substrate, meaning that the MgO crystallite size is influenced by the substrate size [34]. Additionally, the calcination parameters affect the MgO crystallite size even with a constant substrate size. As shown in **Fig. 2 (a)** and **(b)**, no brucite was detected in any groups, indicating the complete decomposition of brucite into reactive magnesia cement (RMC). Moreover, Rietveld refinement results revealed that all groups' MgO content exceeded 91%. The peaks exhibited increased sharpness with higher calcination temperatures, suggesting a tendency towards complete periclase lattice formation [11]. **Fig. 2 (c)** and **(d)** further demonstrate a decrease in the full width at half maximum (FWHM) and an increase in crystallite size (G_{xrd}) with elevated calcination temperatures.

The calcination of $Mg(OH)_2$ involves the release of H_2O, resulting in MgO with a porous structure. Increasing the calcination temperature beyond the decomposition point of $Mg(OH)_2$ leads to the sintering of MgO, reducing its porosity and increasing its crystallite size [35]. When comparing S4-1 and S4-2 to S5-1 and S5-2, the crystallite size (G_{xrd}) of the latter increased by 19% and 30%, respectively. However, further increasing the calcination temperature did not significantly raise G_{xrd}. Meanwhile, for RMC-CC, the changes between SS5.5-0.5, SS5-0.5, and SS5 were smaller than those between SS5 and SS4.5. This indicates that 500 °C is a critical point, after which the rate of increase in G_{xrd} decreases with further temperature rise, consistent with the findings in reference [14].

View Article Online
DOI: 10.1039/D5GC03502C

3.1.2 Morphologies

Fig. 3 (a)-(f) illustrates the microscopic morphology of RMC-TC. During the calcination process, internal moisture diffused outward, creating a mass transfer channel (**Fig. 3 (i)**). Brucite became loose due to lattice distortion [36], a process requiring time. As shown in (**Fig. 3 (a)-(b)**), S4-1 and S4-2 exhibited high packing density and low porosity within the specimen due to insufficient heat transfer [14].

As the calcination temperature increased, RMC particles gradually transformed from plate-like to spherical shapes and became more dispersed [14], resulting in decreased packing density and enhanced RMC reactivity. Additionally, the morphology of RMC-CC is shown in **Fig. 3 (g)-(h)**. SS4 had an irregular plate-like structure, similar to S4-1 and S4-2. Meanwhile, the over-calcined SS7-6 displayed significantly larger particle sizes (mostly 50-300 nm) compared to all others (mostly 20-100 nm).

3.1.3 Specific surface area (SSA) and particle size

Fig. 4 (a) and **(b)** illustrate the SSA of RMC-TC and RMC-CC. For RMC-TC, 500 °C was identified as the threshold temperature. When the calcination temperature was the same, increasing the calcination time from 1 h to 2 h had a negligible effect on the SSA, ranging from -8% to 6%. Additionally, compared to S4-1 and S4-2, S5-1 and S5-2 demonstrated a more regular atomic arrangement in the MgO crystal lattice, resulting in decreased crystal defects [37]. Furthermore, these samples exhibited increased MgO grain size, leading to a 41% and 46% reduction in SSA compared to S4-1 and S4-2, respectively.

However, the SSA decreased only slightly as the calcination temperature increased further. Specifically, the SSA of S6-1 and S6-2 decreased by only 6% and 3% compared to S5-1 and S5-2, respectively. For RMC-CC, the SSA of SS4 (~77.0 m^2/g) was the highest among

all groups and was close to the highest SSA (~78.8 m²/g) reported by Dong et al. [35], indicating that a high-SSA RMC could be obtained through the complete calcination scheme. The most rapid decrease in SSA in the 400-550 °C range occurred at 450 °C, with SS450 exhibiting a 33% decrease in SSA compared to SS4.

The decrease in SSA of SS5-0.5 was slight compared to SS5. Due to the prolonged cooling period (~1 day) of RMC-CC, there was sufficient time for heat transfer, rendering the increase in holding time of 0.5 hours negligible in effect on SSA. SS7-6 exhibited the largest crystallite size, highest crystallinity, and fewest defects [37, 38], thus indicating the smallest SSA (~17.4 m²/g). Furthermore, comparing the properties of RMC-TC and RMC-CC, it is evident that the complete calcination scheme can improve RMC SSA.

Fig. 4 (c) demonstrates the particle size distribution of RMC-TC. The strong van der Waals forces between nanoscale RMC particles led to their agglomeration, resulting in particle size at the micrometer level, significantly larger than the nanometer-level crystallite size Gxrd. As shown in **Fig. 4 (d)**, the D50 of RMC-TC first decreased and then increased with rising calcination temperatures. S4-1 and S4-2 exhibited higher packing density, facilitating particle aggregation and resulting in a larger D50 than S5-1 and S5-2. Conversely, the D50 of S6-1 and S6-2 was higher than that of S5 and S4 due to their advanced crystal development. Additionally, the sintering phenomenon, where small particles converge into larger ones, contributed to the larger D50. **Fig. 4 (e)** shows the macroscopic appearance of SS7-6 with the highest sintering degree, where gaps left by moisture and heat transfer are visible, and the powders adhered to each other.

3.1.4 Reactivity

Fig. 5 (a) depicts the acid neutralization time of RMC-TC. S5-1 exhibited the highest reactivity as its acid neutralization time was the smallest. When the calcination temperature

was the same, different calcination times (1 h or 2 h) had little effect on magnesia reactivity, and the difference between each group was between 9-17%. Moreover, due to the high packing density and low porosity, S4-1 and S4-2 revealed a slower generation rate of Mg^{2+} and OH^- than S5-1 and S5-2, resulting in their longer acid neutralization time (see **Section 3.6.1** for details).

Fig. 5 (b) presents the acid neutralization time of RMC-CC. The acid neutralization time increased with increased calcination degree, indicating that a long cooling time facilitated heat and moisture transfer. Compared to RMC-TC, RMC-CC exhibited a more regular atom array in the MgO crystal lattice and decreased crystal defects, so they demonstrated lower reactivity.

3.2 Mechanical properties of RMC-based mortars

Synthetic RMC and commercial RMC were used to prepare CO_2-cured mortars, and their mechanical properties were measured through compressive strength and nanoindentation testing, as detailed in Section 2.2 for sample preparation and mix design.

3.2.1 Compressive strength

Fig. 6 (a) and **(b)** show the compressive strength of all CO_2-cured mortars after up to 28 days. As shown in **Fig. 6 (a)**, akin to the OPC system [39], the compressive strength of the commercial RMC-based specimens increased as the w/c ratio decreased. C55 achieved the highest compressive strength, with a 28-day strength 1.45 times greater than that of C65. A comparable trend was observed in the synthetic RMC-based specimens, where S5-2-0.85 exhibited the highest compressive strength, while S5-2-1.25 showed the lowest. Additionally, commercial RMC-based mortar demonstrated maximum compressive strength at 7 or 14 days, but excessive expansion of hydration and carbonation products at later stages [40] led to crack formation and reduced strength (see the figure in the discussion section).

Consequently, extending the curing time weakened the strength: the 28-day compressive strength of C55, C60, and C65 decreased by 21.8%, 16.1%, and 16.3%, respectively, compared to the 7-day strength. Hay [41] reported a similar phenomenon that due to the excessive carbonation caused by volume expansion, the compressive strength of RMC-based material decreased by ~11.1% at 28 days compared to 14 days under 20% CO_2 curing.

Fig. 6 (b) demonstrates the effectiveness of using synthetic RMC to enhance the mechanical properties of RMC-based mortar. C55, S4-2-1.25, and S5-2-0.85 exhibited similar working performance. S5-2-0.85 achieved the highest 28-day compressive strength among all groups, which was 15% higher than that of C55. Furthermore, high-reactivity RMC led to a higher degree of hydration and carbonation, resulting in a positive correlation between compressive strength and RMC reactivity when the w/c ratio was kept constant (w/c=1.25).

3.2.2 Elastic modulus and hardness

Fig. 7 and **Fig. S2** illustrate the contour maps and frequency distributions of moduli/hardness in the aggregates, interfacial transition zone (ITZ), and paste of S5-2-1.25, S6-2-1.25, S5-2-0.85, and C55. The areas were divided into aggregates, ITZ, and paste based on color differences in the contour maps. The ITZ width was approximately 30 μm, consistent with reference [42]. Additionally, the ITZ and paste of S6-2-1.25 exhibited a dark blue color, indicating low elastic modulus and hardness. In the S6-2-1.25 group, 97.6% of the elastic modulus values in the paste and ITZ were less than 30 MPa. In contrast, 83.3% of the values in the S5-2-0.85 group were greater than 30 MPa, and 7.1% exceeded 60 MPa, indicating the formation of more high-density HMC. This trend was similarly reflected in the hardness measurements.

View Article Online
DOI: 10.1039/D5GC03302C

Table S2 and **Fig. S3** provide detailed distributions of elastic modulus and hardness along the X-axis, along with the values for each phase in S5-2-1.25, S6-2-1.25, S5-2-0.85, and C55. S5-2-0.85 and S6-2-1.25 exhibited the highest and lowest elastic modulus and hardness in the paste and ITZ, respectively, aligning with their overall mechanical properties.

Previous studies reported that the elastic modulus of ITZ was smaller than that of the paste in air-cured OPC mortar with a w/c ratio of 0.53 [42]. Furthermore, compared to air curing, CO_2 curing enhances ITZ performance as CO2 diffuses along the ITZ [18], leading to substantial HMC formation in the ITZ. Therefore, despite the higher w/c ratios in our study (0.55-1.25 vs. 0.53), the elastic modulus and hardness of the ITZ were close to or even exceeded that of the paste [42].

3.3 Hydration/carbonation degrees of RMC-based mortars

The measurement of hydration and carbonation degrees in RMC-based mortar can reflect its strength development.

Fig. 8 illustrates the XRD patterns of all groups after 3 and 14 days of CO_2 curing. Compared to the commercial RMC-based specimens, the synthetic RMC-based specimens exhibited more intense brucite peaks and weaker periclase peaks, indicating a faster hydration rate for the synthetic RMC. Additionally, the quartz peaks present in all groups originated from sand, and the magnesite peaks were from the commercial RMC material. Furthermore, due to the preferential formation of nesquehonite in high-concentration CO_2 environments [43], only nesquehonite was observed, rather than hydromagnesite and dypingite. The formation of nesquehonite is also influenced by pH levels and the presence of HCO_3^- [44], as detailed in the discussion section.

Table S3 shows the unhydrated MgO and uncarbonated brucite contents in all groups,

View Article Online
DOI: 10.1039/D5GC03502C

obtained through RIR. The MgO content decreases in all groups from 3 to 14 days due to increased hydration. High-reactivity RMC demonstrated a faster hydration rate and lower MgO content. Specifically, the high-reactivity S5-1-1.25 and S5-2-1.25 exhibited the lowest MgO content, and the synthetic RMC-based groups showed a smaller MgO content than the low-reactivity commercial RMC-based groups.

Fig. 9 illustrates the TG-DTG curves of all specimens at 3 and 14 days. The three main phase decomposition stages are listed below [2]:

50-300 °C: Dehydration of water bonded to HMCs (e.g., nesquehonite, hydromagnesite and dypingite).

300-500 °C: Dehydroxylation of HMCs (e.g., hydromagnesite and dypingite), decarbonation of HMCs (e.g., nesquehonite) and decomposition of uncarbonated brucite.

500-900 °C: Decarbonation of HMCs (e.g., nesquehonite, magnesite, hydromagnesite and dypingite).

The mass loss across three temperature ranges is shown in **Table 3**. The synthetic RMC-based group exhibited average mass loss increases of 4.5%, 5.5%, and 0.9% at 50-300 °C, 300-500 °C, and 500-900 °C, respectively, over 3 to 14 days. In contrast, the commercial RMC-based group showed negligible mass loss growth in these temperature ranges due to its significantly lower reactivity compared to the synthetic counterparts. This result aligns with the RIR findings, which indicated higher brucite and HMC content in the synthetic RMC-based group compared to the commercial one.

3.4 Pore structure of RMC-based mortars

The pore structure of mortar significantly impacts its mechanical properties and durability [45]. **Fig. 10** presents the 2D X-ray computed tomography (X-CT) images of selected groups at 14 days. Aggregates in concrete mitigate the expansion effects of cement, but this constraint is less effective in mortar due to the absence of aggregates. Consequently, excessive expansion of brucite and HMC caused cracks in the S4-2-1.25 and S5-2-1.25 groups (red circles in **Fig. 10 (a)-(f)**).

The random stacking and hydrogen bonding of brucite [46] resulted in a poorly connected network structure with widely distributed pores throughout S6-2-1.25. Additionally, numerous pores were observed at the interfacial transition zone (ITZ) (yellow circles in **Fig. 10 (g)-(i)** and **(m)**), which weakened the bonding force between the fine aggregate and the paste, leading to stress concentration under load and resulting in the worst mechanical performance for S6-2-1.25. Furthermore, a paste layer (yellow rectangle) was found at the upper part of S6-2-1.25, formed by surplus slurry containing small sand particles that floated to the surface. In contrast, due to the low water-to-cement ratio (w/c), S5-2-0.85 and C55 exhibited dense structures with some trapped pores (blue circles in **Fig. 10 (m)-(o)**).

Fig. 11 (a)-(e) shows the 3D X-CT images of the selected groups at 14 days. The macropores in S4-2-1.25, S5-2-1.25, and S6-2-1.25 were interconnected and extended from the surface to the interior, providing pathways for CO_2 diffusion and further carbonation of the specimens. In contrast, the pores in S5-2-0.85 and C55 were mainly trapped pores. Larger pores lead to stress concentration and decreased concrete strength. As depicted in **Fig. 11 (f)**, the order of mortar mechanical properties aligns with the pore structure parameters: the 28-day compressive strength was highest in S5-2-0.85 and lowest in S6-2-1.25.

View Article Online
DOI: 10.1039/D5GC03502C

3.5 Carbon footprint

The carbon emission equivalent for commercial RMC and wet synthesis RMC is shown in **Fig. 11 (g).** The carbon emissions for commercial RMC are 1.53 kg CO_2 eq, which is similar to the average value reported in the literature [1]. In contrast, the carbon emissions from the wet synthesis process of RMC are higher, 15.0% greater than those of commercial RMC. The higher carbon emissions are mainly attributed to the production of the alkaline source CaO, which is used to precipitate $Mg(OH)_2$ from waste brine solutions. The production of CaO involves the calcination of $CaCO_3$, which generates a significant amount of CO_2, leading to a high carbon footprint. This process emits ten times more CO_2 than the calcination of $Mg(OH)_2$ and other subsequent treatments. However, the RMC synthesized using the parameters in this study results in a carbon emission equivalent that is 18.9% lower than the wet synthesis carbon emission equivalents reported in other literature (1.76 kg CO_2 eq vs. 2.17 kg CO_2 eq) [1].

Since the production of CaO is the primary contributor to the significant carbon footprint of wet-synthesized RMC, the total CO_2 emissions can be further reduced from RMC production by using alternative alkaline sources [47]. This approach is not only more sustainable but also more cost-effective. Additionally, a large volume of brine is required because the concentration of Mg^{2+} ions in the brine used in this study is relatively low. In the future, the concentration of Mg^{2+} ions in the brine could be increased through green energy methods such as solar evaporation, which would reduce the amount of brine required per cycle and indirectly decrease CO_2 emissions from subsequent processes like washing and centrifugation.

When assessing the net CO_2 emissions of RMC-based binders, an important aspect is the amount of CO_2 that can be absorbed during the use phase of their concrete products. Specifically, the net CO_2 emissions should be calculated. The RMC produced through the

wet process has higher purity and reactivity than RMC produced by the calcination of magnesite [48]. Most existing literature studies typically stop at comparing the carbon emissions of RMC cement produced through two different methods, without considering the subsequent CO_2 capture in concrete. This study expands on this by extending the analysis to mortar-based applications and recalculating the net CO_2 emission equivalent, as detailed in the discussion.

3.6 Discussion

3.6.1 Key factors Influencing the reactivity of RMC

(a) Statistical analysis of reactivity versus SSA of RMC

Fig. 12 (a) illustrates the fitting curve between the acid neutralization time and SSA of RMC-CC. A higher SSA indicates more surface sites are available for interaction with water, leading to increased Mg^{2+} dissolution and subsequent formation of magnesium hydroxide [48]. Consequently, there is a strong correlation between the RMC neutralization time and SSA, with an R^2 value of 0.91.

In contrast, **Fig. 12 (b)** and **(c)** show the fitting curves of RMC's acid neutralization time and SSA from references [12, 14]. Researchers [12] used a maximum calcination temperature and duration of 700 °C for 12 hours, respectively, resulting in RMC with a lower SSA (<10 m²/g) and poorer reactivity (>2200 s). As shown in **Fig. 12 (b)**, when the SSA is < 15 m²/g, the acid neutralization time increases rapidly with decreasing SSA. This led to the fitting functions in the two studies being represented by an inverse proportional function (**Fig. 12 (b)**) and an exponential function (**Fig. 12 (c)**), respectively. It should be noted that compared to references [12] and [14], the effective high-temperature calcination time (> 400 °C) for RMC-CC in this study is shorter, resulting in a higher SSA (mostly >20 m²/g) and better RMC reactivity. Consequently, the fitting function for this study is linear, differing from those in references [12] and [14].

View Article Online
DOI: 10.1039/D5GC03502C

Fig. 12 (d) shows scatter plots of acid neutralization time versus SSA for RMC-TC. The poor-fitting relationship observed is due to the fact that high-SSA RMC-TC samples, such as S4-1 and S4-2, exhibited longer acid neutralization times compared to S5-1 and S5-2. Nonetheless, as mentioned earlier, a good-fitting relationship between acid neutralization time and SSA was observed when RMC was fully calcined. Therefore, it can be predicted that data points for calcination temperatures between 500-600 °C and durations of 1-2 hours will be located near the red dashed line (ideal fitting line).

(b) Crystal phase transformation during calcination of brucite

RMC reactivity is not only related to particle size, but also to phase transition [14, 49-51]. The thermal decomposition process of $Mg(OH)_2$ is illustrated in **Fig. 13** (a). During the thermal decomposition, partial dehydroxylation occurred between the layers of $Mg(OH)_2$, forming $Mg_xO_y(OH)_{2x-2y}$, as shown in Eq. (5) [49]. As the temperature increases or calcination time is prolonged, dehydroxylation proceeds until it is complete, leading to the formation of MgO crystals. At low temperatures and short calcination durations, the dominant exposed plane in the resulting MgO is the (111) plane. This plane is highly unstable due to its low atomic density, which correlates with higher reactivity. At this stage, MgO crystallizes in a hexagonal system (space group $P6_3mc$ (186)). With further heat treatment, the (111) plane transitions into the (100), (010), and (001) planes. The flake-like crystals subsequently transform into MgO with a stable polyhedral cubic crystal structure (space group Fm-3m (225)), leading to a reduction in the specific surface area (SSA) of the crystal particles [50, 51].

$$xMg(OH)_2 \rightarrow Mg_xO_y(OH)_{2x-2y} + yH_2O \quad (5)$$

Rietveld whole-pattern fitting refinement was performed on the XRD data of S4-2, S5-2, and S6-2, with the results shown in **Fig. 13** (b). S4-2 exhibited the highest proportion of MgO ($P6_3mc$ (186)), which correlated with its largest specific surface area (SSA) among the three groups. As the temperature increased, the unstable, highly reactive layered MgO crystals

gradually transformed into stable cubic structures. Consequently, S6-2 was composed almost entirely of cubic MgO.

View Article Online
DOI: 10.1039/D5GC03502C

As shown in **Fig. 13 (c)**, the MgO crystallites grew progressively larger as the calcination temperature increased. At 400°C, although the obtained RMC retained more layered structures, its intergranular porosity was relatively low. During calcination at 500°C, $Mg(OH)_2$ dehydroxylation proceeded more rapidly, leading to the formation of larger crystallites. The rapid dehydroxylation process also resulted in increased intergranular porosity, allowing the reactant solution to access more active sites within the MgO powder. At 600°C, the high temperature facilitated the rapid formation of MgO crystals, which became more structurally regular, thereby reducing both SSA and intergranular porosity.

3.6.2 Key factors Influencing the strength of RMC-based specimens

Considering the above, it is necessary to discuss the correlation between the mechanical strength of RMC-based mortar and various influencing factors: material-level (RMC reactivity) and specimen-level (ITZ characteristics, porosity, and hydration/carbonation degree). The degree of hydration/carbonation was represented by the unhydrated MgO content and the weight loss during the 300-500 °C range in the TG test [17]. Additionally, given the limited increase in hydration/carbonation degree and strength development from 14 to 28 days [17, 18], the microscopic test results at 14 d were selected for analysis.

(a) Material-level properties

When the water-to-cement ratio (w/c) was kept constant at 1.25, the 28-day compressive strength of the synthetic RMC-based mortar exhibited a strong correlation with RMC reactivity (reciprocal of acid neutralization time), with an R^2 value of 0.91 (**Fig. 14 (a)**). The high-reactivity RMC group demonstrated a greater degree of hydration and carbonation, resulting in more carbonation products (HMCs) that reduced porosity and improved the ITZ

characteristics of the mortar, thereby enhancing its mechanical properties, consistent with the findings of Mi et al [52]. Mi et. al [52] also observed that under air-curing conditions, high-activity RMC-based mortars rapidly formed expansion products (such as brucite), which led to crack formation and subsequent deterioration of strength. Consequently, air-cured RMC-based samples showed a negative correlation between compressive strength and RMC reactivity.

(b) Specimen-level properties

Fig. 14 (b)-(d) illustrates that the 28-day compressive strength of the specimens shows a significant correlation with specimen porosity and the modulus/hardness of the ITZ. Lower specimen porosity decreases the likelihood of pore evolution into large cracks under stress concentration. Additionally, a higher elastic modulus and hardness of the ITZ result in slower crack development at the ITZ under the same loading conditions, leading to a more gradual decline in specimen stiffness. Thus, reduced porosity and enhanced ITZ characteristics both contribute to improved mechanical properties of the specimens.

When the w/c was constant at 1.25, the correlation coefficient (R^2) between the 28-day compressive strength and the hydration/carbonation degree was higher than the R^2 values at different w/c ratios (0.85, 1.05, and 1.25). Since the latter correlations were not statistically significant at the 0.05 level, **Fig. 14 (e)** and **(f)** only present the fitting results for the constant w/c ratio. Additionally, at a constant w/c of 1.25, a lower unhydrated MgO content allowed for more carbonation of hydration products, resulting in greater HMC formation. Consequently, specimen porosity decreased, and the modulus/hardness of the ITZ was strengthened, leading to increased compressive strength [18, 53].

However, when w/c ratios varied (0.85, 1.05 and 1.25), an increased w/c promoted hydration and carbonation reactions, reducing the unhydrated MgO content. Additionally, a high w/c

resulted in a thicker coating of water, which expanded the interspaces among cement particles and left coarser capillary pores after being filled by hydration products. High w/c also increased porosity and ITZ width while reducing the elastic modulus of the paste and ITZ [42]. Therefore, the strength was influenced by multiple factors when w/c ratios varied, significantly weakening its correlation with the hydration/carbonation degree.

(c) Pairwise relationships between properties of material- and specimen-level

In addition to analyzing the correlation between strength and various factors, it is also necessary to examine the pairwise relationships between material properties, specimen mechanical properties, and hydration/carbonation degrees. **Table 4** demonstrates the correlation coefficients between six factors in synthetic RMC-based mortar with the same w/c ratio. Although the 14-day and 28-day compressive strengths of CO_2-cured RMC-based mortars showed a significant correlation with RMC reactivity, they had no significant correlation with SSA ($p > 0.05$). This is because high-SSA S4-1 and S4-2 exhibited lower reactivity than S5-1 and S5-2, resulting in limited strength improvement in S4-1-1.25 and S4-2-1.25. Additionally, the carbonation degree was positively correlated with the hydration degree. When the w/c ratio is constant, higher RMC reactivity leads to more hydration products available for carbonation, thereby improving the carbonation degree and enhancing the mortar's strength. This explains the significant correlation between strength and the degrees of hydration and carbonation.

When expanding the data range to include groups with low-activity commercial RMC and different w/c ratios, the pairwise correlation coefficients between six factors in RMC-based mortar are shown in **Table 5**. In RMC-based mortar, the 28-day strength exhibited a strong correlation with the 14-day strength, as did the carbonation degree with the hydration degree. (**Fig. 15 (a)**). However, the strength is no longer significantly correlated with the degree of hydration/carbonation. Conversely, as high-SSA synthetic RMC and low-SSA commercial

RMC exhibit high and low hydration/carbonization degrees, respectively, the correlation between the degree of hydration/carbonization and SSA is enhanced (**Fig. 15 (b)** and **(c)**).

View Article Online
DOI: 10.1039/D5GC03502C

3.6.3 Carbonation degrees versus mineral phases/net carbon footprint of RMC-based specimens

(a) Carbonation degrees versus mineral phases

Nesquehonite was preferentially generated in low pH environments rich in HCO_3^- [44]. According to XRD and TG-DTG results, synthetic RMC-based mortars exhibited a higher degree of carbonation and consequently a lower pH environment compared to commercial RMC-based mortars. In this low pH environment, many carbonate ions exist in the form of CO_3^{2-}, and the presence of more HCO_3^- facilitated the formation of nesquehonite [44]. Therefore, only nesquehonite was observed in synthetic RMC-based mortars, rather than hydromagnesite or dypingite. Additionally, nesquehonite peaks were significantly more pronounced in synthetic RMC-based mortars than in commercial RMC-based mortars. Furthermore, compared to concrete, mortar lacks coarse aggregates, which hinders CO_2 diffusion [54], and contains more RMC, indicating a greater degree of carbonation than concrete [2].

(b) Carbonation degrees versus net carbon footprint

The optimal compressive strength group for commercial RMC/synthetic RMC is selected as C55/S5-2-0.85. A 1-ton mortar model is established for each, considering the CO_2 absorption during mixing, demolding, and accelerated carbonation curing. The net carbon emissions of the two mortar groups are calculated, with the mixture of 1-ton mortar provided in **Table S4** in supplement document.

Existing literature indicates that the carbon sequestration capacity of RMC varies due to factors such as CO_2 concentration, pressure, and carbonation time. For example, under flue

gas treatment at 120°C and 0.4 MPa, the carbon sequestration rate of RMC is 20 g CO_2 per 100 g of sample [55, 56]. The carbon sequestration rate of the two mortar samples prepared in the laboratory was calculated and scaled up to 1 ton of mortar. A model was established to calculate the net CO_2 emissions for the production of 1 ton of mortar (**Fig. 16**).

In this experiment, the carbonation curing environment of the samples has not yet reached optimal parameters. As a result, the carbon emissions for the synthetic MgO-based mortar group are slightly higher than those for the commercial RMC-based mortar group. Due to the different water-to-binder ratios used in the mortars, the CO_2 intensity data is provided to more clearly link the compressive strength with carbon emissions for both groups. As shown in **Fig. 16**, the CO_2 emissions per MPa for the synthetic MgO-based mortar were 19.7% lower than those for the commercial RMC-based mortar. Moreover, the theoretical CO_2 absorption capacity of synthetic MgO can reach approximately 110% [20]. It indicated that the net carbon emissions and carbon intensity of synthetic MgO-based mortar could be further reduced by using additives, adjusting mix proportions and optimizing curing conditions [2, 56], thus highlighting its advantages over dry-route RMC-based mortar.

4 Conclusions

This study investigated the production and application of RMC extracted from bischofite via the wet route, involving two calcination schemes: timed calcination and complete calcination. The physicochemical properties of synthetic RMC were analyzed. Mortar samples were prepared using synthetic RMC obtained by timed calcination and subjected to 28 days of CO_2 curing, and compared to those involving commercial RMC (produced via the dry route). The phase composition, pore structure, and ITZ characteristics were examined, leading to several key findings:

(1) For synthetic RMC obtained by complete calcination, a robust correlation between acid

View Article Online
DOI: 10.1039/D5GC03302C

neutralization time and SSA was observed (R^2 = 0.91). As calcination temperature increased, the MgO lattice became more complete, grain size (G_{XRD}) increased, SSA decreased, and acid neutralization time increased. RMC obtained by calcining brucite at 500°C for 1 or 2 hours exhibited the highest reactivity among all groups.

(2) The mechanical properties of mortars improved with a decreased w/c ratio, reflected in the strength order of both commercial and synthetic RMC-based mortars. Due to the smaller particle size and higher SSA of synthetic RMC, its hydration and carbonation rates were significantly faster than those of commercial RMC.

(3) Compared to commercial RMC, the use of high-activity synthetic RMC improved the mechanical properties of CO_2-cured mortars. At a constant w/c ratio, high-reactivity RMC showed higher hydration and carbonation rates, resulting in a denser pore structure and improved ITZ performance. Thus, the 28-day compressive strength of synthetic RMC-based mortar was closely associated with RMC reactivity, ITZ elastic modulus/hardness, porosity, and unhydrated MgO content. These relationships could allow for the accurate prediction and precise control of RMC-based mortar performance at both material and specimen levels.

(4) RMC synthesized in this study exhibited an equivalent carbon emission 18.9% lower than those reported in the literature. Besides, when the carbon sequestration potential of RMC was considered, the carbon emissions for the synthetic RMC-based mortars were lower than those for the commercial RMC-based samples. CO_2 intensity data further showed that synthetic RMC-based mortars emitted 19.7% less CO_2 per MPa compared to commercial RMC-based samples.

Further research is required to enhance the production and purity of MgO in the wet process through process optimization. Additionally, an improved calcination method should be

established to utilize heat from the cooling stage while mitigating the adverse effects of prolonged insulation time on RMC reactivity.

View Article Online
DOI: 10.1039/D5GC03502C

Author contributions

Yufeng Song: Methodology, Investigation, Writing– review & editing

Jiaze Wang: Investigation, Writing – original draft

Xinpeng Wang: Visualization, Methodology

Jiahao Zhou: Investigation, Visualization

Cise Unluer: Conceptualization, Writing– review & editing

Tao Shi: Formal analysis, Writing– review & editing

Aoyun Zhang: Visualization, Investigation

Chenggong Chang: Resource, Investigation

Shaoqin Ruan: Conceptualization, Funding acquisition, Writing – review & editing

Conflicts of interest

There are no conflicts to declare

Data availability

The authors confirm that the data supporting the findings of this study are available within the article and its supplementary materials.

Acknowledgement

The authors acknowledge the National Natural Science Foundation of China (No. 52108255 and 52402036). This work was also financially supported by the "Pioneer" R&D Program of Zhejiang (2022C03003). The authors are grateful for the assistance from Liying Chen at the State Key Laboratory of Modern Optical Instruments (Zhejiang University) for performing the 3D interference microscope. The authors are also grateful for the assistance of Li-Juan Mao, Chaogang Xing and Dongmei Qi for FTIR, XRD and TG-DTG analyses from the Analysis

Center of Agrobiology and Environmental Sciences, Faculty of Agriculture, Life and Environment Sciences (ACAES), Zhejiang University.

View Article Online
DOI: 10.1039/D5GC03502C

Reference

[1] I. Singh, R. Hay, K. Celik, Recovery and direct carbonation of brucite from desalination reject brine for use as a construction material, Cement and Concrete Research, 152 (2022) 106673.

[2] Y. Song, X. Qian, D. Yan, C. Unluer, Y. Peng, D. Kong, C. Hu, S. Wang, S. Ruan, Understanding the role of seeds in reactive magnesia cement (RMC) formulations, Journal of the American Ceramic Society, 106 (2023) 3812-3831.

[3] L. Xu, L. Liu, Z. Fang, M. Chen, G. Ou, M. Suzuki, Y. Sakai, Electrolyte pH modulation for efficient and durable electrochemical cement clinker precursor production, Green Chemistry, 27 (2025) 3706-3714.

[4] A. Font, M.V. Borrachero, L. Soriano, J. Monzó, A. Mellado, J. Payá, New eco-cellular concretes: Sustainable and energy-efficient materials, Green chemistry, 20 (2018) 4684-4694.

[5] N. Dung, C. Unluer, Potential additives for magnesia-based concrete with enhanced performance and propensity for CO_2 sequestration, Journal of CO_2 Utilization, 56 (2021) 101834.

[6] X. Chen, T. Zhang, C. Cheeseman, W. Bi, S. Wang, Production of Rapid-Hardening Magnesium Oxysulfate Cement Containing Boric Acid, Journal of Materials in Civil Engineering, 34 (2022) 04022045.

[7] R. Hay, C. Otchere, G. Kashwani, K. Celik, Recycling carbonated reactive magnesium cement (RMC) as a building material, Journal of Cleaner Production, 320 (2021) 128838.

[8] S. Ruan, C. Unluer, Comparative life cycle assessment of reactive MgO and Portland cement production, Journal of Cleaner Production, 137 (2016) 258-273.

[9] L. An, C. Chang, F. Yan, J. Peng, Study on the Deterioration Mechanism of Magnesium Oxychloride Cement under an Alkaline Environment, Materials, 16 (2023) 5924.

[10] I. Mironyuk, V. Gun'ko, M. Povazhnyak, V. Zarko, V. Chelyadin, R. Leboda, J. Skubiszewska-Zięba, W. Janusz, Magnesia formed on calcination of $Mg(OH)_2$ prepared from natural bischofite, Applied Surface Science, 252 (2006) 4071-4082.

[11] W. Zheng, J. Dong, Y. Li, J. Wen, C. Chang, B. Li, Y. Li, Preparation technology and microstructural changes of low-activity magnesium oxide based on salt lake bischofite, Powder Technology, (2023) 119248.

[12] H. Dong, C. Unluer, E.-H. Yang, A. Al-Tabbaa, Recovery of reactive MgO from reject brine via the addition of NaOH, Desalination, 429 (2018) 88-95.

[13] H. Dong, C. Unluer, E.-H. Yang, A. Al-Tabbaa, Synthesis of reactive MgO from reject brine via the addition of NH4OH, Hydrometallurgy, 169 (2017) 165-172.

[14] S. Chu, E.H. Yang, C. Unluer, Chemical synthesis of magnesium oxide (MgO) from brine towards minimal energy consumption, Desalination, 556 (2023) 116594.

[15] F. Shahbaz, I. Singh, P. Krishnan, K. Celik, Life cycle assessment of brucite and synthetic MgO produced from reject brine using different alkalis, Journal of Cleaner Production, 380 (2022) 135071.

[16] N.H. de Azevedo, P.R. de Matos, P.J. Gleize, A.M. Betioli, Effect of thermal treatment of SiC nanowhiskers on rheological, hydration, mechanical and microstructure properties of Portland cement pastes, Cement and Concrete Composites, 117 (2021) 103903.

[17] N. Dung, C. Unluer, Influence of nucleation seeding on the performance of carbonated MgO formulations, Cement

and Concrete Composites, 83 (2017) 1-9.

[18] Y. Song, J. Wang, Y. Huang, J. Wang, Y. Weng, R. Ma, K.S.H. Pang, S. Ruan, Effects of varying grades/pretreatments of recycled aggregates on the development of pore structures and ITZs within reactive magnesia cement (RMC) concrete, Cement and Concrete Research, 190 (2025) 107782.

[19] P. Badjatya, A.H. Akca, D.V. Fraga Alvarez, B. Chang, S. Ma, X. Pang, E. Wang, Q. Van Hinsberg, D.V. Esposito, S. Kawashima, Carbon-negative cement manufacturing from seawater-derived magnesium feedstocks, Proceedings of the National Academy of Sciences, 119 (2022) 2114680119.

[20] S. Ruan, E.-H. Yang, C. Unluer, Production of reactive magnesia from desalination reject brine and its use as a binder, Journal of CO2 Utilization, 44 (2021) 101383.

[21] T. Zhang, B. Ma, H. Tan, H. Qi, T. Shi, Effect of sodium carbonate and sodium phosphate on hydration of cement paste, Journal of Building Engineering, 45 (2022) 103577.

[22] L. Rouchon, L. Favergeon, M. Pijolat, Analysis of the kinetic slowing down during carbonation of CaO by CO2, Journal of Thermal Analysis and Calorimetry, 113 (2013) 1145-1155.

[23] YB/T 4019—2020 Determination of chemical activity of light calcined magnesia [S], Beijing, 2020.

[24] GB/T 2419-2005 Test method for fluidity of cement mortar, Beijing, 2005.

[25] C. Pan, Y. Song, J. Wang, S. Zhan, C. Unluer, S. Ruan, Unlocking the role of recycled aggregates in the performance enhancement and CO_2 capture of reactive magnesia cement formulations, Cement and Concrete Research, 168 (2023) 107148.

[26] Y. Song, M. Dong, Z. Wang, X. Qian, D. Yan, S. Shen, L. Zhang, G. Sun, J. Lai, S. Ruan, Effects of red mud on workability and mechanical properties of autoclaved aerated concrete (AAC), Journal of Building Engineering, (2022) 105238.

[27] K. Gu, Y. Maierdan, B. Chen, Effects of ethylenediamine tetra-acetic acid (EDTA) and its disodium salt derivative (EDTA-Na) on the characteristics of magnesium oxysulfate (MOS) cement, Composites Part B: Engineering, 232 (2022) 109654.

[28] K. Gu, L. Lang, D. Li, B. Chen, Preparation of Magnesium Oxysulfate Cement with Calcined Phosphate Tailings, Journal of Materials in Civil Engineering, 34 (2022) 04022358.

[29] J.M. Montero, P. Gai, K. Wilson, A.F. Lee, Structure-sensitive biodiesel synthesis over MgO nanocrystals, Green chemistry, 11 (2009) 265-268.

[30] S.S. Owoeye, Grace Olufunke Matthew, Faith Osesenaga Ovienmhanda, S.O. Tunmilayo, Preparation and characterization of foam glass from waste container glasses and water glass for application in thermal insulations, Ceram. Int., 46 (2020) 11770-11775.

[31] C. Unluer, A. Al-Tabbaa, Characterization of light and heavy hydrated magnesium carbonates using thermal analysis, J. Therm. Anal. Calorim., 115 (2014) 595-607.

[32] M. Liska, A. Al-Tabbaa, Ultra-green construction: reactive magnesia masonry products, Proceedings of the Institution of Civil Engineers-Waste and Resource Management, Thomas Telford Ltd, 2009, pp. 185-196.

[33] Y. Song, Y. Zhang, S. Shen, C. Pan, D. Yan, Z. Wang, S. Wang, S. Ruan, Effects of $Ca(OH)_2$ on the reinforcement corrosion of sulfoaluminate cement mortar, Materials and Structures, 56 (2023) 26.

[34] J. Li, Y. Zhang, S. Shao, S. Zhang, Comparative life cycle assessment of conventional and new fused magnesia production, Journal of Cleaner Production, 91 (2015) 170-179.

[35] A.A. Pilarska, Ł. Klapiszewski, T. Jesionowski, Recent development in the synthesis, modification and application

of Mg (OH) 2 and MgO: A review, Powder Technology, 319 (2017) 373-407.

[36] H. Dong, E.-H. Yang, C. Unluer, F. Jin, A. Al-Tabbaa, Investigation of the properties of MgO recovered from reject brine obtained from desalination plants, Journal of cleaner production, 196 (2018) 100-108.
View Article Online
DOI: 10.1039/D5GC03502C
[37] R. Salomão, C.C. Arruda, M.L. Antunes, Synthesis, dehydroxylation and sintering of porous $Mg(OH)_2$-MgO clusters: Evolution of microstructure and physical properties, Interceram-International Ceramic Review, 69 (2020) 52-62.

[38] L. Mo, M. Deng, M. Tang, Effects of calcination condition on expansion property of MgO-type expansive agent used in cement-based materials, Cement and Concrete Research, 40 (2010) 437-446.

[39] L. Huang, Z. Yang, S. Wang, Influence of calcination temperature on the structure and hydration of MgO, Construction and Building Materials, 262 (2020) 120776.

[40] S. Singh, P. Munjal, N. Thammishetti, Role of water/cement ratio on strength development of cement mortar, Journal of Building Engineering, 4 (2015) 94-100.

[41] L. Pu, C. Unluer, Investigation of carbonation depth and its influence on the performance and microstructure of MgO cement and PC mixes, Construction and Building Materials, 120 (2016) 349-363.

[42] R. Hay, K. Celik, Hydration, carbonation, strength development and corrosion resistance of reactive MgO cement-based composites, Cement and Concrete Research, 128 (2020) 105941.

[43] Y. Gao, C. Hu, Y. Zhang, Z. Li, J. Pan, Characterisation of the interfacial transition zone in mortars by nanoindentation and scanning electron microscope, Magazine of Concrete Research, 70 (2018) 965-972.

[44] E.G. Soares, J. Castro-Gomes, Carbonation curing Influencing factors of carbonated reactive magnesia cements (CRMC)–a review, Journal of Cleaner Production, 38 (2021) 127210.

[45] S. Ruan, J. Qiu, Y. Weng, Y. Yang, E.-H. Yang, J. Chu, C. Unluer, The use of microbial induced carbonate precipitation in healing cracks within reactive magnesia cement-based blends, Cement and Concrete Research, 115 (2019) 176-188.

[46] R. Martínez-García, M.S. de Rojas, P. Jagadesh, F. López-Gayarre, J.M. Morán-del-Pozo, A. Juan-Valdes, Effect of pores on the mechanical and durability properties on high strength recycled fine aggregate mortar, case studies in construction materials, 16 (2022) e01050.

[47] Z. Li, J. Qian, J. Qin, Y. Hua, Y. Yue, H. Tang, Cementitious and hardening properties of magnesia (MgO) under ambient curing conditions, Cement and Concrete Research, 170 (2023) 107184.

[48] D.N. Huntzinger, J.S. Gierke, S.K. Kawatra, T.C. Eisele, L.L. Sutter, Carbon dioxide sequestration in cement kiln dust through mineral carbonation, Environmental Science and Technology, 43 (2009) 1986-1992.

[49] F. Jin, A. Al-Tabbaa, Characterisation of different commercial reactive magnesia, Advances in cement research, 26 (2014) 101-113.

[50] A.V.G. Chizmeshya, M.J. McKelvy, R. Sharma, R.W. Carpenter, H. Bearat, Density functional theory study of the decomposition of Mg(OH)2: a lamellar dehydroxylation model, Materials Chemistry and Physics, 77 (2003) 416-425.

[51] M. Kitagawa, S. Misu, J. Ichikawa, H. Matsuhashi, Preparation of active MgO by short-time thermal decomposition of Mg (OH) 2, Research on Chemical Intermediates, 41 (2015) 9463-9473.

[52] G.A. Mutch, S. Shulda, A.J. McCue, M.J. Menart, C.V. Ciobanu, C. Ngo, J.A. Anderson, R.M. Richards, D. Vega-Maza, Carbon capture by metal oxides: unleashing the potential of the (111) facet, Journal of the American Chemical Society, 140 (2018) 4736-4742.

[53] T. Mi, E.-H. Yang, C. Unluer, Investigation of the properties of reactive MgO-based cements and their effect on performance, Cement and Concrete Composites, 138 (2023) 104984.

[54] X. Diao, Y. Song, S. Pan, X. Cai, T. Shi, L. Wang, Enhanced dynamic compressive performance of silicon carbide whiskers-modified mortars, Construction and Building Materials, 432 (2024) 136626.

[55] M. Sereng, A. Djerbi, O.O. Metalssi, P. Dangla, J.-M. Torrenti, Improvement of recycled aggregates properties by means of CO2 uptake, Applied Sciences, 11 (2021) 6571.

[56] K. Rausis, A. Ćwik, I. Casanova, Phase evolution during accelerated CO2 mineralization of brucite under concentrated CO2 and simulated flue gas conditions, Journal of CO2 Utilization, 37 (2020) 122-133.

[57] D. Meng, C. Unluer, E.-H. Yang, S. Qian, Recent advances in magnesium-based materials: CO2 sequestration and utilization, mechanical properties and environmental impact, Cement and Concrete Composites, 138 (2023) 104983.

List of Tables

Table 1 Details of timed and complete calcination.

View Article Online
DOI: 10.1039/D5GC03502C

Calcination regime	Synthetic RMC category	Group	The maximum temperature (°C)	The maximum temperature duration (h)	Cooling time (d)
Timed calcination	RMC-TC	S4-1	400	1	0
		S4-2	400	2	0
		S5-1	500	1	0
		S5-2	500	2	0
		S6-1	600	1	0
		S6-2	600	2	0
Complete calcination	RMC-CC	SS4	400	0	1
		SS4.5	450	0	1
		SS5	500	0	1
		SS5-0.5	500	0.5	1
		SS5.5-0.5	550	0.5	1
		SS7-6	700	6	1

View Article Online
DOI: 10.1039/D5GC03502C

Table 2 Mixture formulations of RMC-based mortar specimens.

Group	RMC	RMC/sand ratio	w/c
C55	Commercial RMC	2:3	0.55
C60			0.60
C65			0.66
S4-1-1.25	Synthetic RMC	2:3	1.25
S4-2-1.25			
S5-1-1.25			
S5-2-1.25			
S6-1-1.25			
S6-2-1.25			
S5-2-1.05	Synthetic RMC	2:3	1.05
S5-2-0.85			0.85

Table 3 Mass loss of specimens at 3 d and 14 d obtained by TG-DTG (wt.%).

Group	50-300 °C		300-500 °C		500-900 °C	
	3 d	14 d	3 d	14 d	3 d	14 d
S4-1-1.25	9.45	15.04	18.42	25.29	2.06	2.92
S4-2-1.25	8.07	14.00	17.49	24.33	2.11	3.23
S5-1-1.25	9.32	15.68	20.63	27.13	1.92	3.19
S5-2-1.25	8.95	15.18	18.06	24.85	2.14	3.32
S6-1-1.25	6.32	8.35	18.08	22.23	2.03	3.01
S6-2-1.25	5.86	9.32	17.38	20.15	1.91	2.26
S5-2-1.05	7.43	12.56	17.21	23.71	2.00	3.02
S5-2-0.85	8.17	9.88	17.65	22.48	1.96	3.34
C55	4.89	5.45	8.28	8.61	1.77	1.82
C60	5.62	6.13	9.58	9.68	2.22	2.34
C65	6.63	6.76	10.39	10.47	1.85	2.27

Table 4 Pearson correlation coefficient between 6 factors in synthetic RMC-based mortar with the same w/c ratio.

Pearson correlation coefficients	RMC properties		Mechanical properties		Hydration degree	Carbonation degree
	Reactivity (s^{-1})	SSA (m^2/g)	14 d f'_c (MPa)	28 d f'_c (MPa)	14 d MgO content (wt.%)	14 d Weight loss (wt.%)
Reactivity (s^{-1})	1	0.084	**0.876***	**0.932****	**-0.817***	**0.933****
SSA (m^2/g)		1	0.494	0.288	-0.379	0.326
14 d f'_c (MPa)			1	**0.965****	**-0.925****	**0.941****
28 d f'_c (MPa)				1	**-0.915***	**0.915***
14 d MgO content (wt.%)					1	**-0.921****
14 d Weight loss (wt.%)						1

Note: (1) ** and * represent significance levels, $p \leq 0.05$ and $p \leq 0.01$, respectively; (2) Weight loss is the weight difference of 300-500 °C in TG-DTG curves.

Table 5 Pearson correlation coefficient between 6 factors in synthetic/commercial RMC-based mortars with different w/c ratios.

Pearson correlation coefficients	RMC properties		Mechanical properties		Hydration degree	Carbonation degree
	Reactivity (s^{-1})	SSA (m^2/g)	14 d f'_c (MPa)	28 d f'_c (MPa)	14 d MgO content (wt.%)	14 d Weight loss (wt.%)
Reactivity (s^{-1})	1	0.583	0.129	0.111	**-0.835****	**0.877****
SSA (m^2/g)		1	-0.310	-0.399	**-0.784****	**0.810****
14 d f'_c (MPa)			1	**0.989****	0.328	-0.303
28 d f'_c (MPa)				1	0.362	-0.343

14 d MgO content (wt.%)		1	**-0.981****
14 d Weight loss (wt.%)			1

Note: (1) ** and * represent significance levels, $p \leq 0.05$ and $p \leq 0.01$, respectively; (2) Weight loss is the weight difference of 300-500 °C in TG-DTG curves.

List of Figures

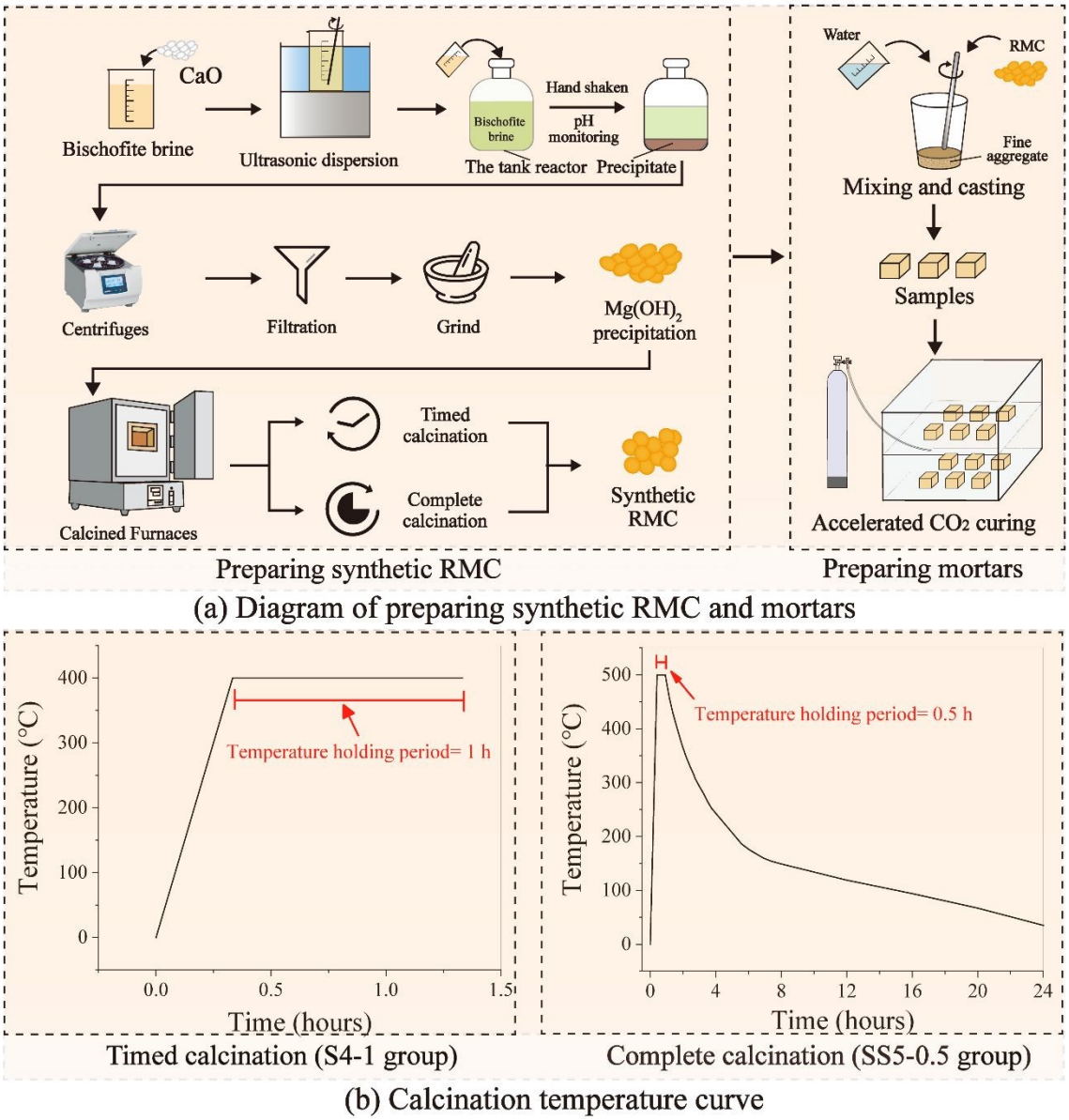

Fig. 1 (a) Diagram showing the preparation of synthetic RMC and mortars and (b) Calcination temperature curve of S4-1 and SS5-0.5 over time.

View Article Online
DOI: 10.1039/D5GC03502C

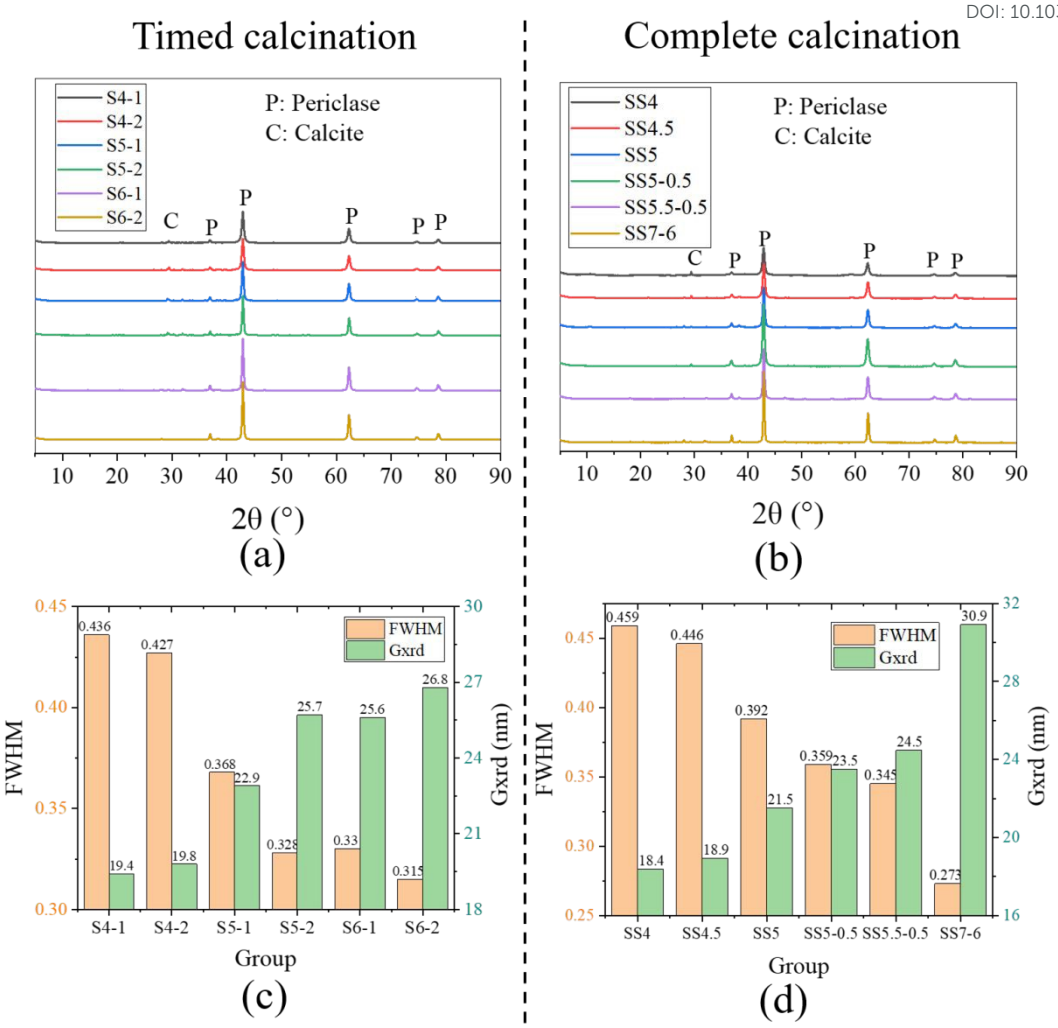

Fig. 2 (a)-(b) XRD patterns, (c)-(d) FWHM and G_{xrd} of RMC-TC and MC-CC.

View Article Online
DOI: 10.1039/D5GC03502C

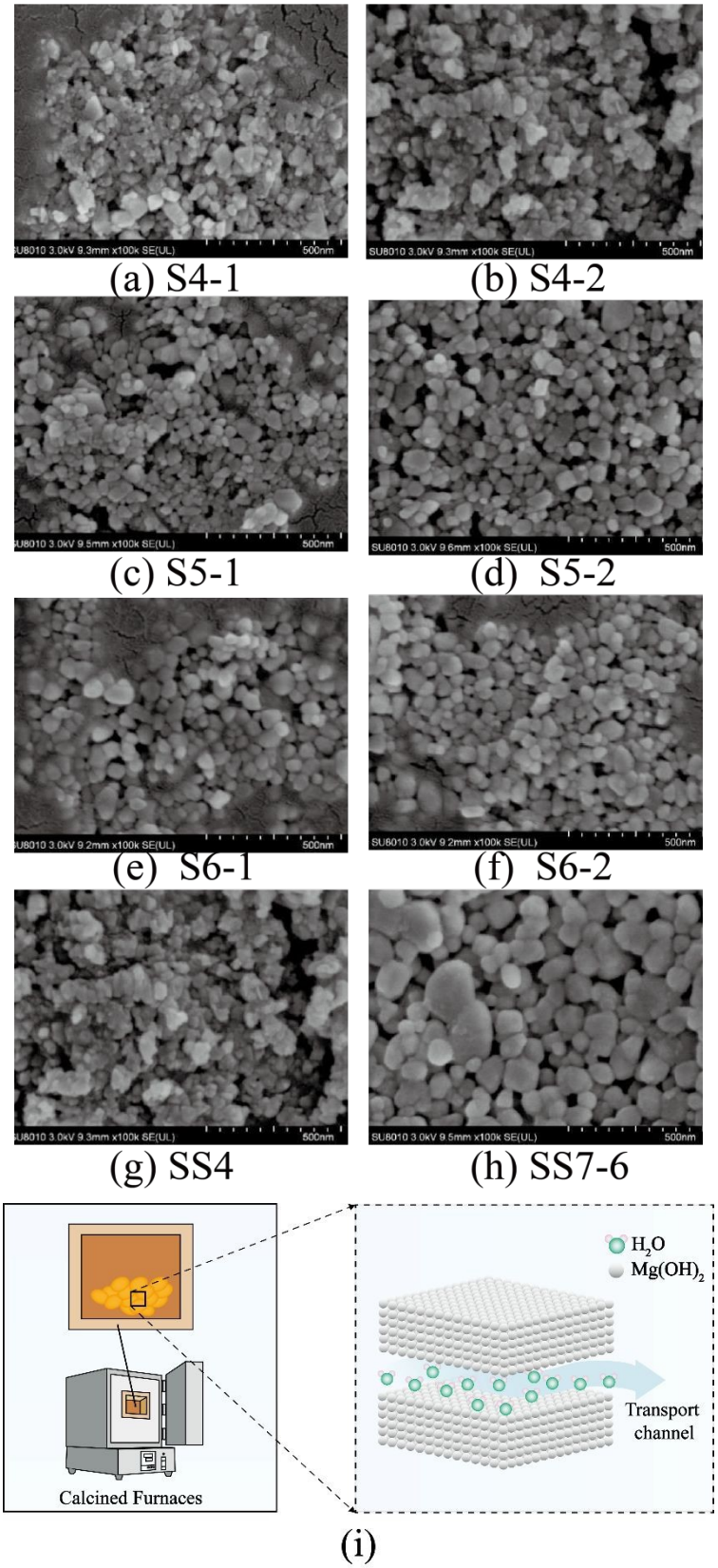

Fig. 3 Microscopic morphologies of (a)-(f) RMC-TC and (g)-(h) RMC-CC; (i) schematic diagram of moisture diffusion during the brucite calcination process.

View Article Online
DOI: 10.1039/D5GC03502C

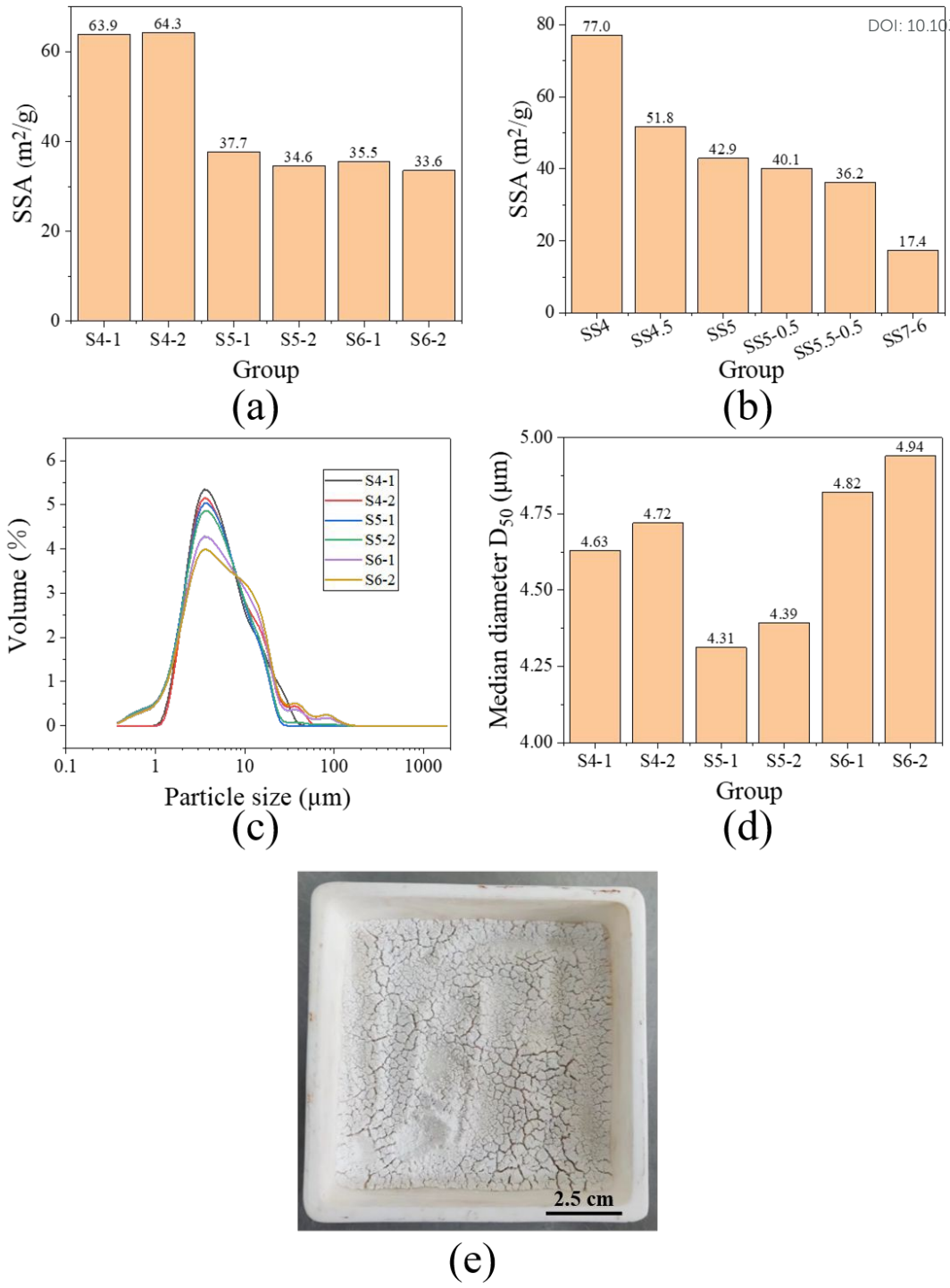

Fig. 4 SSA of (a) RMC-TC and (b) RMC-CC, (c) particle size distribution and (d) median particle size D_{50} of RMC-TC, (e) sintering phenomenon observed in SS7-6.

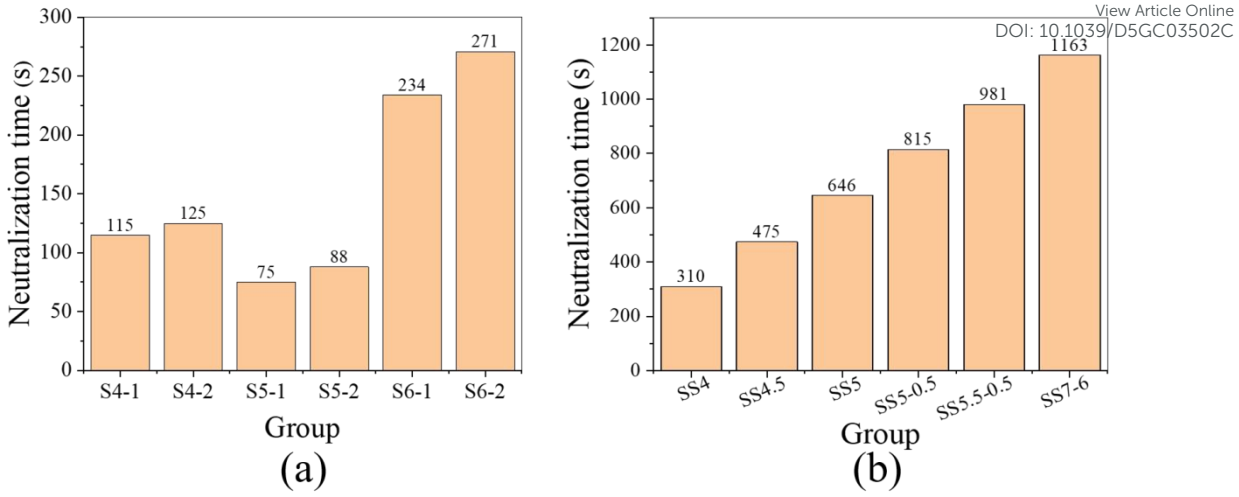

Fig. 5 Acid neutralization time of (a) RMC-TC and (b) RMC-CC.

View Article Online
DOI: 10.1039/D5GC03502C

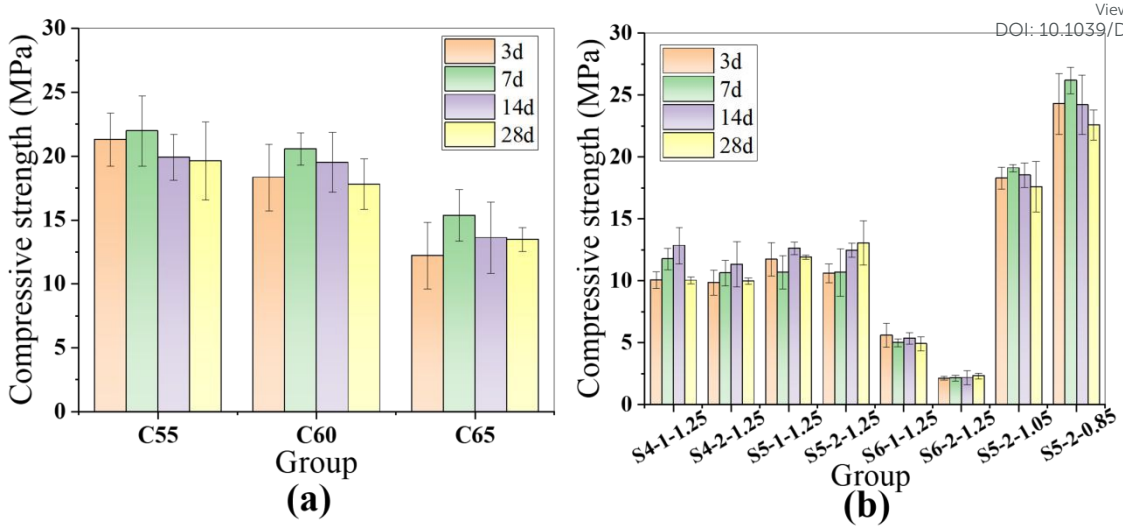

Fig. 6 Compressive strength of all groups with commercial/synthetic RMC after being CO_2-cured for up to 28 d.

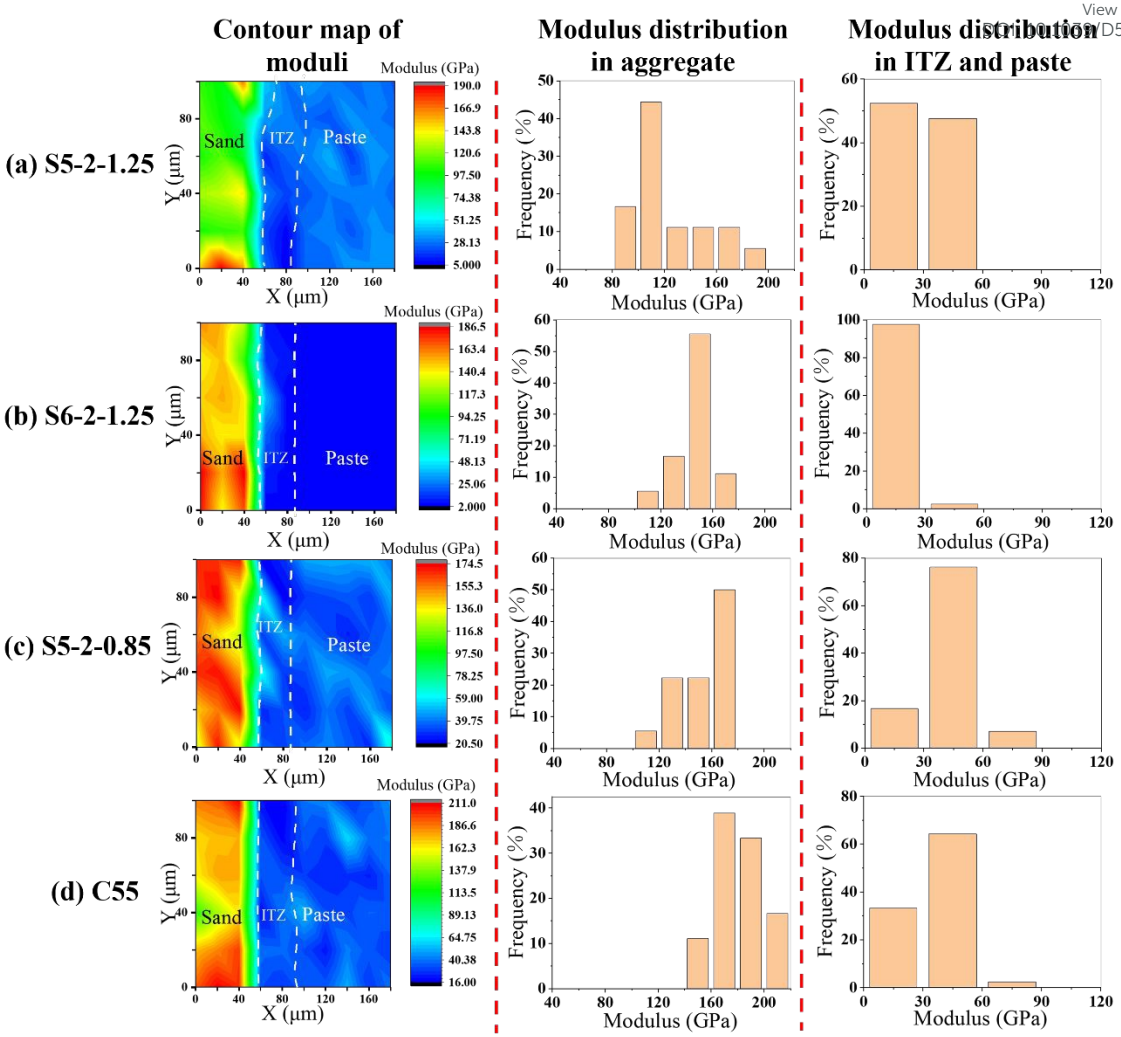

Fig. 7 Moduli contour maps and frequency in aggregates, ITZ and paste of S5-2-1.25, S6-2-1.25, S5-2-0.85 and C55.

View Article Online
DOI: 10.1039/D5GC03502C

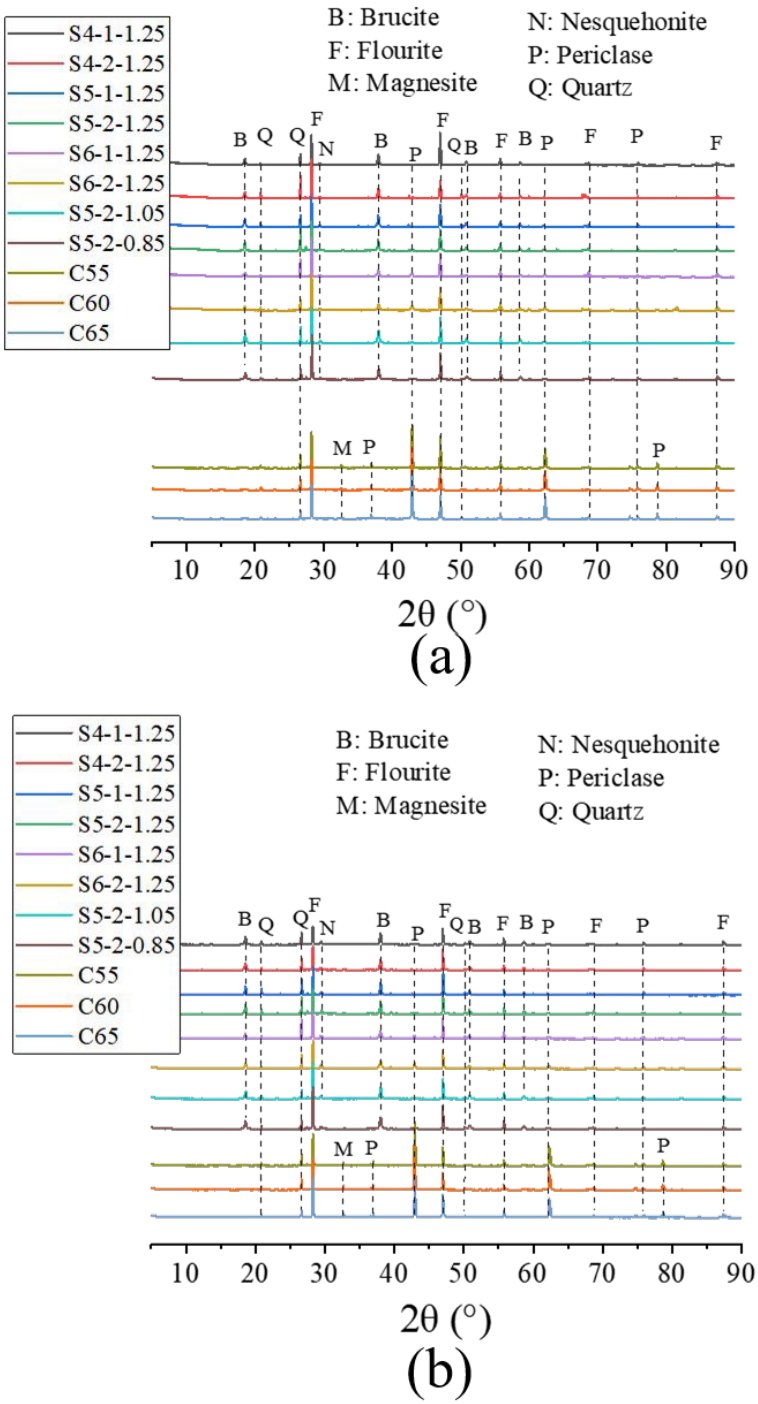

Fig. 8 XRD patterns of all groups after being CO_2-cured for (a) 3 d and (b) 14 d.

View Article Online
DOI: 10.1039/D5GC03502C

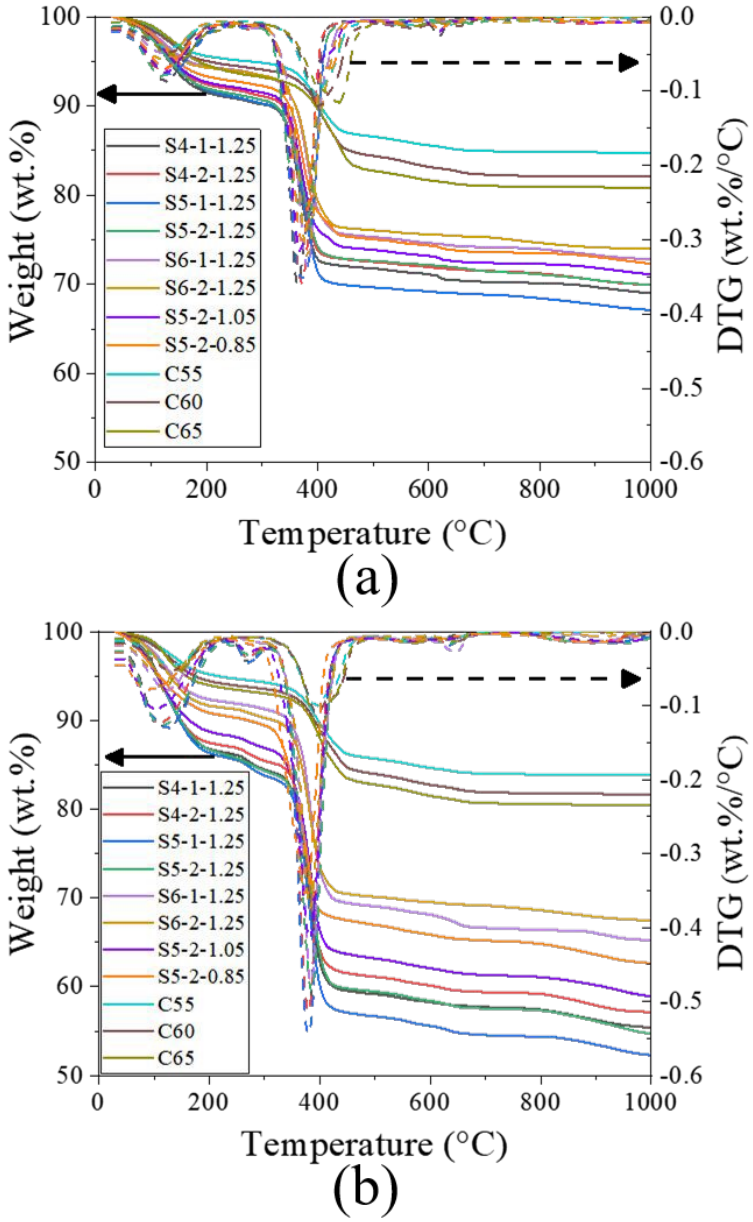

Fig. 9 TG-DTG curves of all groups after being CO_2-cured for (a) 3 d and (b) 14 d.

View Article Online
DOI: 10.1039/D5GC03502C

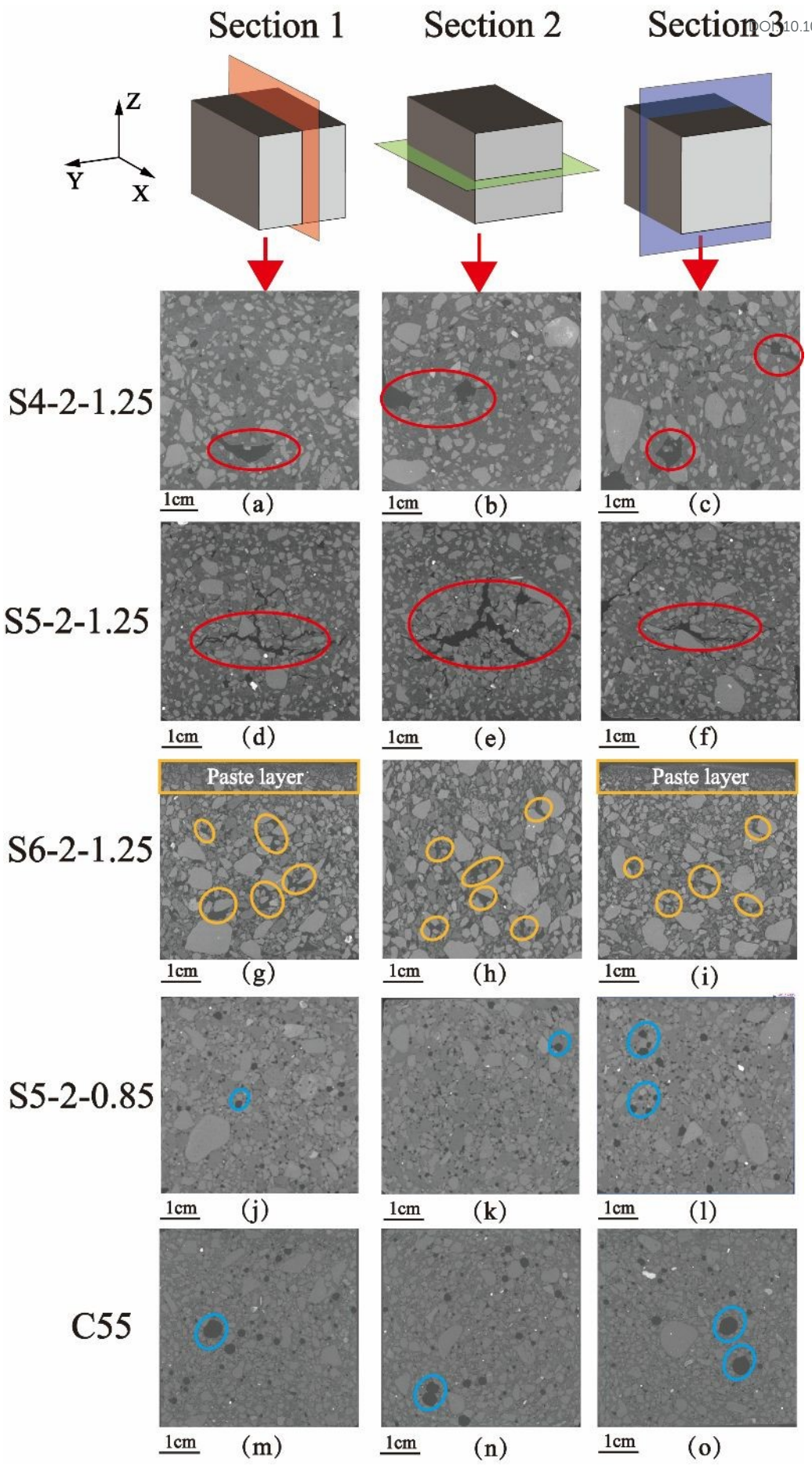

View Article Online
DOI: 10.1039/D5GC03502C

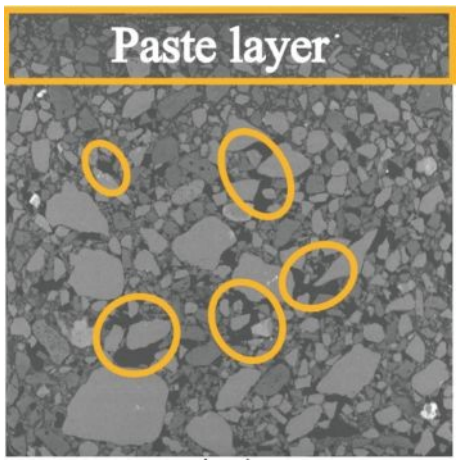

(p) Detail display of S6-2-1.25 (figure (g))

Fig. 10 2D X-CT images of selected groups after being CO_2-cured for 14 d.

View Article Online
DOI: 10.1039/D5GC03502C

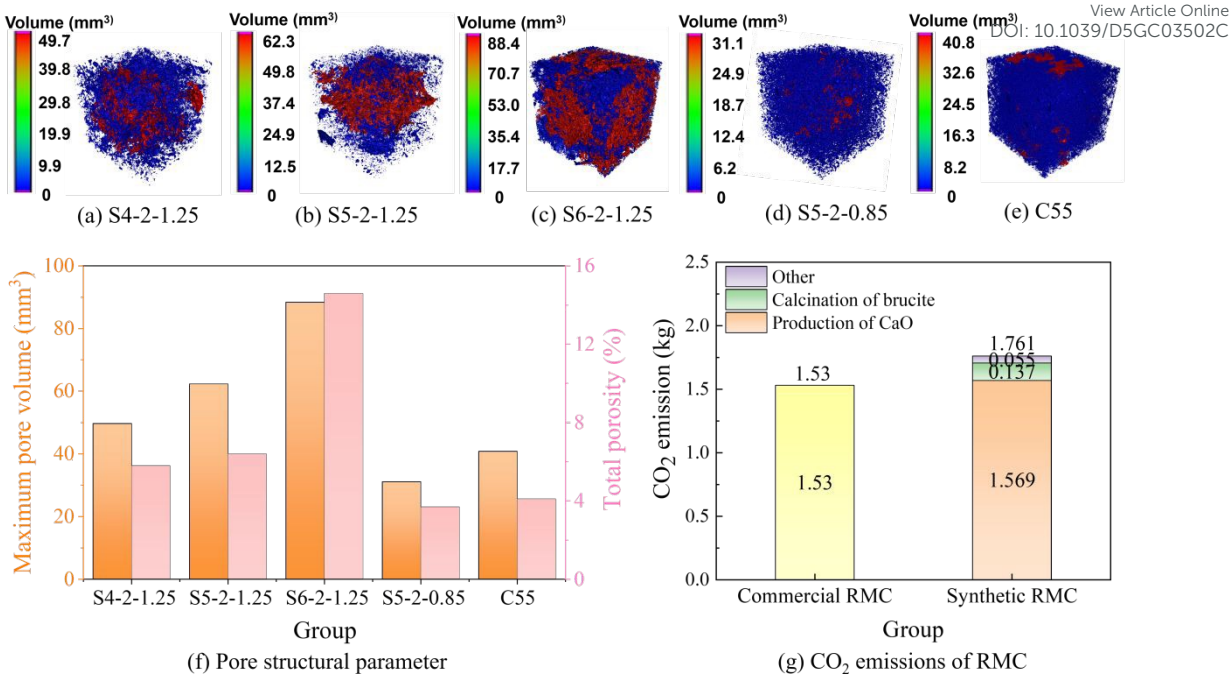

Fig. 11 (a)-(e) 3D images and (f) maximum pore volume and total porosity of selected groups after being CO_2-cured for 14 d; (g) CO_2 emissions associated with the production of 1 kg of synthetic RMC and commercial RMC.

View Article Online
DOI: 10.1039/D5GC03502C

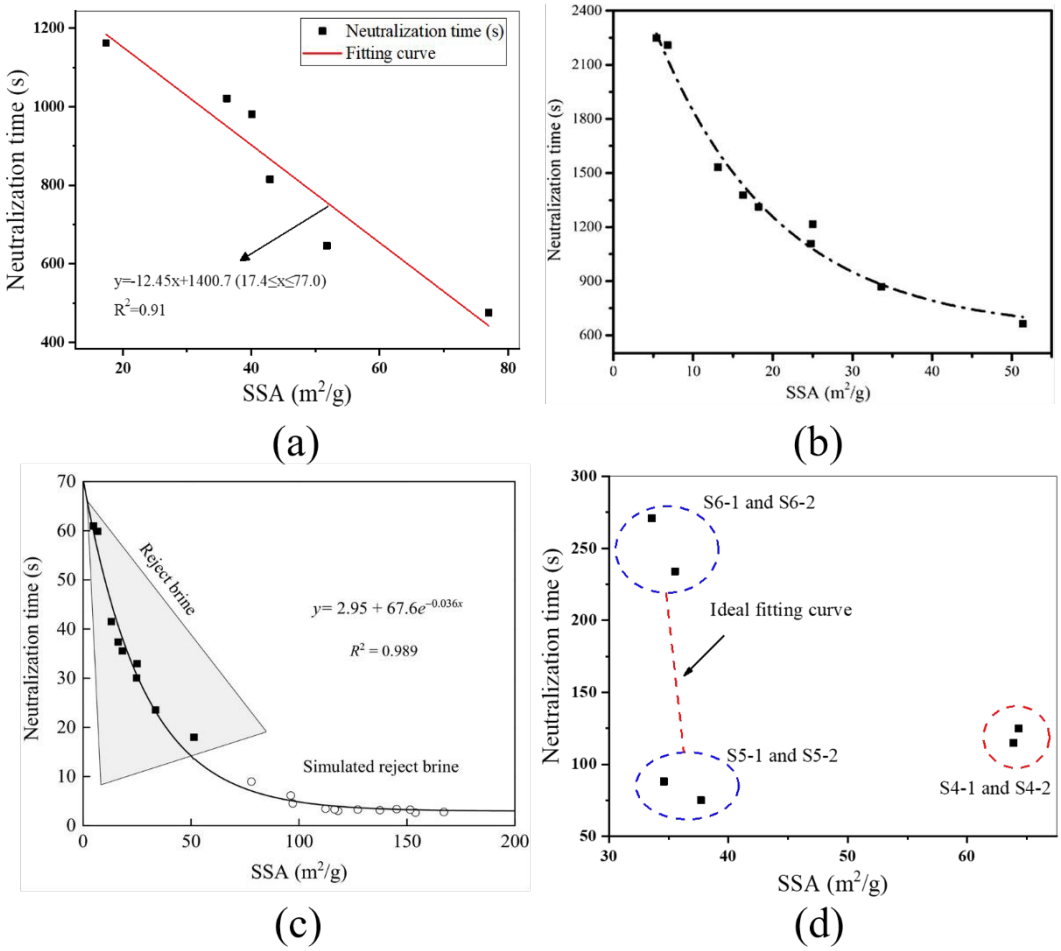

Fig. 12 Fitting curves of RMC' acid neutralization time and SSA: (a) RMC-CC in this study; (b) reference [12] and (c) reference [14]; (d) Scatter plot of RMC-TC.

View Article Online
DOI: 10.1039/D5GC03502C

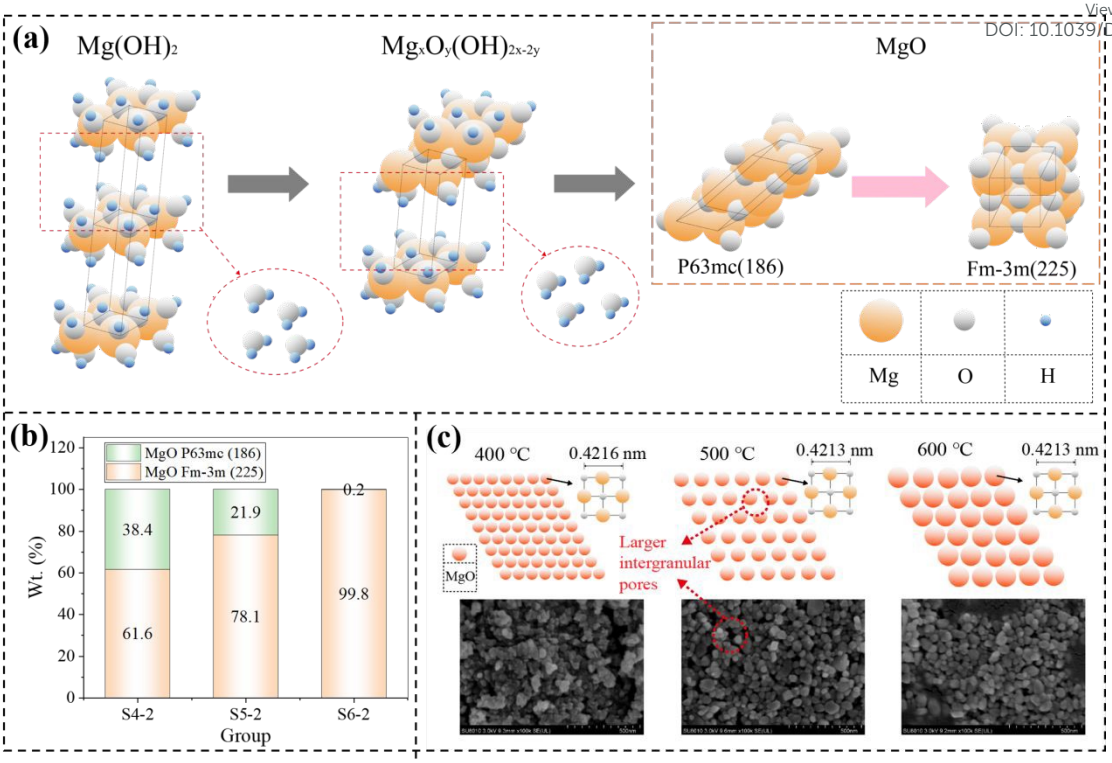

Fig. 13 (a) Schematic diagram of thermal decomposition of magnesium hydroxide, (b) MgO content of different crystal structures in each group of samples and (c) Schematic diagram of different intergranular pores of MgO crystal obtained by decomposition at different temperatures.

View Article Online
DOI: 10.1039/D5GC03502C

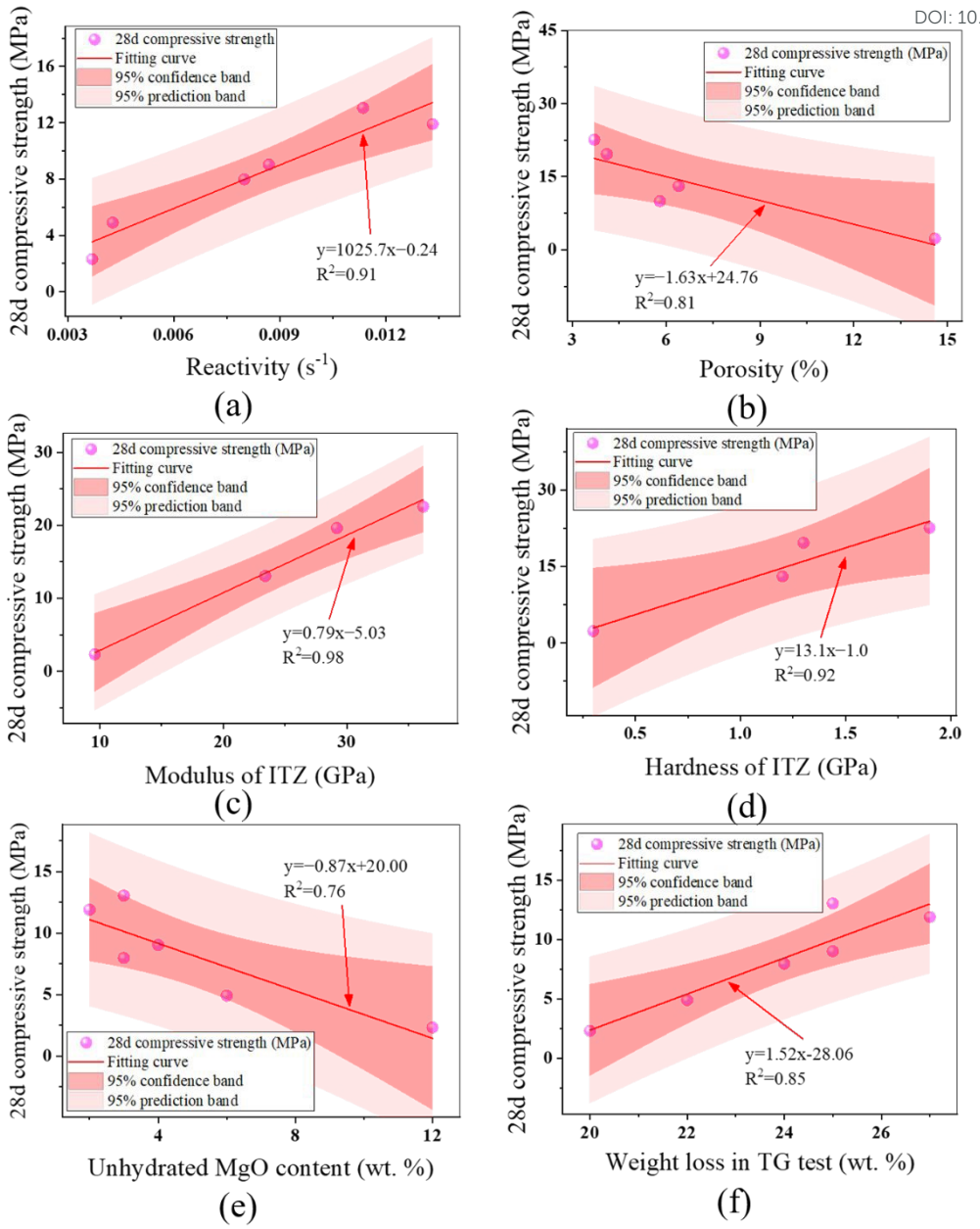

Fig. 14 Fitting curves of 28 d compressive strength and (a) RMC reactivity; (b) porosity; (c) ITZ modulus; (d) ITZ hardness; (e) unhydrated MgO content and (f) weight loss during 300-500 °C in the TG test.

View Article Online
DOI: 10.1039/D5GC03502C

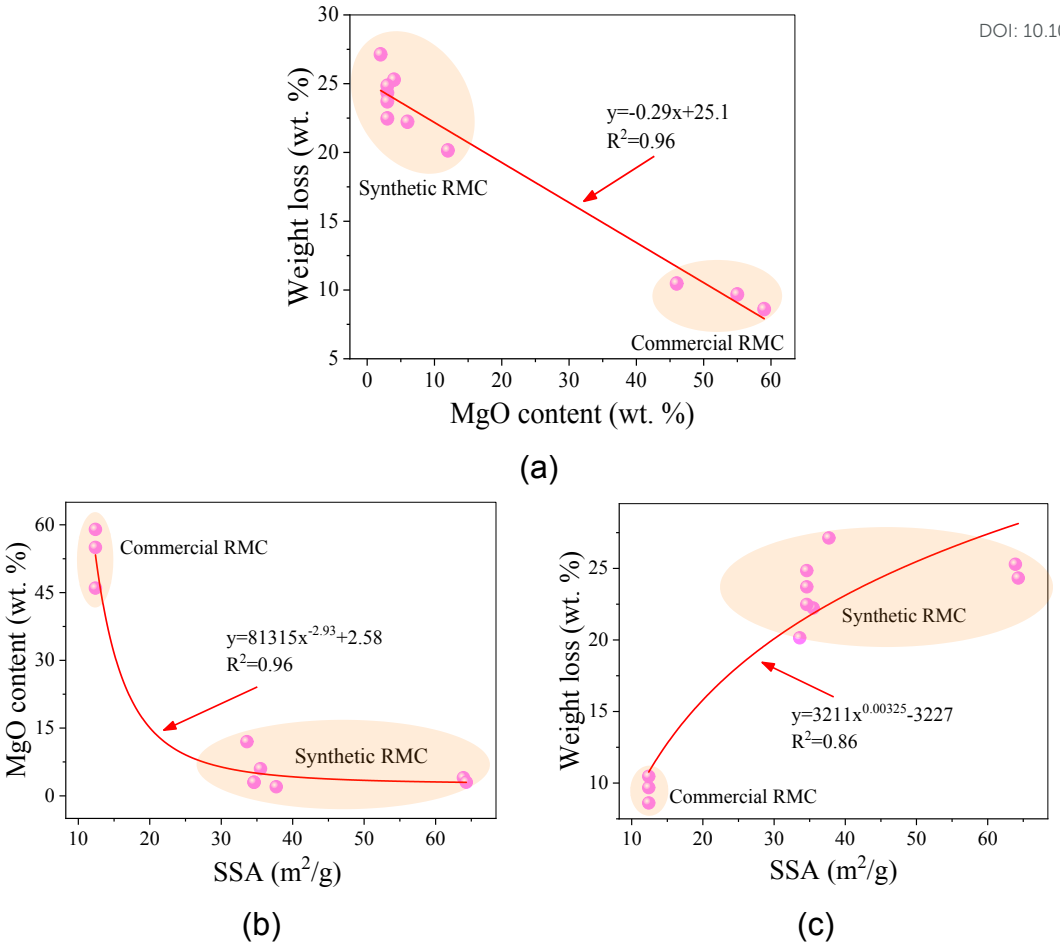

Fig. 15 (a) Fitting curves of synthetic/commercial RMC-based mortars' (a) weight loss (from the TG test) and MgO content; (b) MgO content and SSA; (c) weight loss (from the TG test) and SSA.

View Article Online
DOI: 10.1039/D5GC03502C

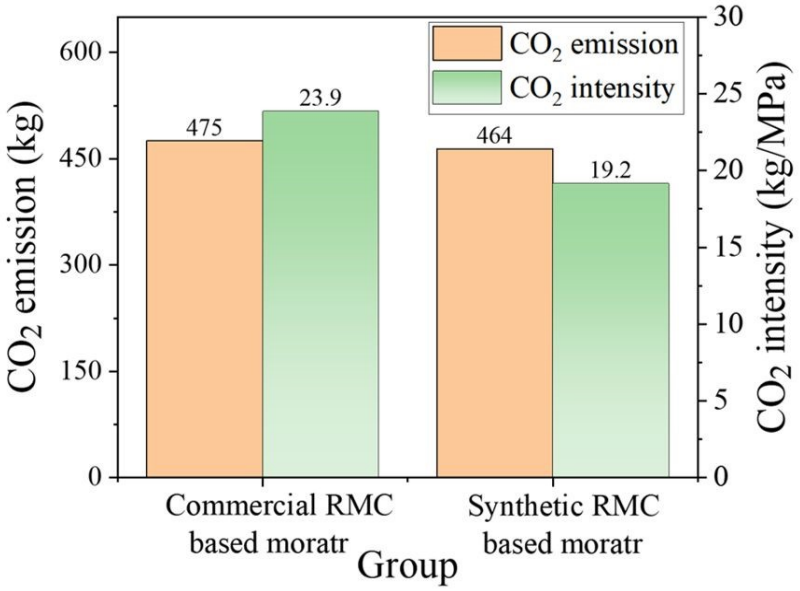

Fig. 16 CO_2 emissions and CO_2 intensity associated with the production of 1 ton of commercial (C55) and synthetic (S5-2-0.85) RMC-based mortar.

View Article Online
DOI: 10.1039/D5GC03502C

Data availability

The authors confirm that the data supporting the findings of this study are available within the article and its supplementary materials.